Physics and Engineering Science                                    College of Science

12-28-2023

# Numerical Study of Owls' Leading-edge Serrations

Asif Shahriar Nafi
*Coastal Carolina University*

Nikolaos Beratlis
*Arizona State University*

Elias Balaras
*George Washington University*

Roi Gurka
*Coastal Carolina University*

## Recommended Citation

# Numerical study of owls' leading-edge serrations

Asif Shahriar Nafi ✉ ⓘ ; Nikolaos Beratlis ⓘ ; Elias Balaras ⓘ ; Roi Gurka ⓘ

Check for updates

CrossMark

View Online

Export Citation

# Numerical study of owls' leading-edge serrations

View Online      Export Citation      CrossMark

Asif Shahriar Nafi,[1,a)] (iD) Nikolaos Beratlis,[2] (iD) Elias Balaras,[3] (iD) and Roi Gurka[1] (iD)

### AFFILIATIONS

[1]Department of Physics and Engineering Science, Coastal Carolina University, Conway, South Carolina 29526, USA
[2]School for Engineering of Matter, Transport and Energy, Arizona State University, Tempe, Arizona 85281, USA
[3]Mechanical and Aerospace Engineering, George Washington University, Washington, District of Columbia 20052, USA

[a)]Author to whom correspondence should be addressed: anafi@coastal.edu

### ABSTRACT

Owls' silent flight is commonly attributed to their special wing morphology combined with wingbeat kinematics. One of these special morphological features is known as the leading-edge serrations: rigid miniature hook-like patterns found at the primaries of the wings' leading-edge. It has been hypothesized that leading-edge serrations function as a passive flow control mechanism, impacting the aerodynamic performance. To elucidate the flow physics associated with owls' leading-edge serrations, we investigate the flow-field characteristic around a barn owl wing with serrated leading-edge geometry positioned at 20° angle of attack for a Reynolds number of 40 000. We use direct numerical simulations, where the incompressible Navier–Stokes equations are solved on a Cartesian grid with sufficient resolution to resolve all the relevant flow scales, while the wing is represented using an immersed boundary method. We have simulated two wing planforms: with serrations and without. Our findings suggest that the serrations improve suction surface flow by promoting sustained flow reattachment via streamwise vorticity generation at the shear layer, prompting weaker reverse flow, thus augmenting stall resistance. Aerodynamic performance is negatively impacted due to the shear layer passing through the serration array, which results in altered surface pressure distribution over the upper surface. In addition, we found that serrations increase turbulence level in the downstream flow. Turbulent momentum transfer near the trailing edge increased due to the presence of serrations upstream the flow, which also influences the mechanisms associated with separation vortex formation and its subsequent development over the upper surface of the wing.

## I. INTRODUCTION

Owls are widely known for their silent flight. Most owl species nocturnal raptors can fly silently, while the diurnal owl species generate sound during their flights akin to any other bird species. The silent owl species have three distinctive wing microfeatures that set them apart from the other non-silent birds including the diurnal owl species. These unique wing features are referred to as leading-edge (LE) combs/serrations that are rigid miniature hook-like patterns located at the leading edge of their wings at an angle to the freestream, they are only present at some primary feathers that form the LE; trailing-edge (TE) fringes, which are soft, flexible hair-like extensions of their feathers (both primary and secondary feathers) located at the trailing edge of their wings; and velvety upper surface that is comprised of elongated soft filaments (known as pennulae) projected from the upper surface of their wings (Graham, 1934; Kroeger *et al.*, 1972). Most owls have relatively bigger wings compared to their body mass (i.e., low wing loading), which allows them to fly without spending much effort (i.e., low wingbeat frequency) (Wagner *et al.*, 2017; Nafi *et al.*, 2020; and

Krishnan, 2022). Despite being large, some of the owl species can even hover for a short duration of time (e.g., barn owl, short eared owl, great gray owl, etc.). These aerodynamic performances make them a potential candidate for bioinspired design research, in particular, for the design improvement of unmanned air vehicle (UAV) wings as they operate at the similar Reynolds number range.

UAVs can be of three types: rotary wing type, fixed wing type, and hybrid. Each of the types has its own advantages and limitations. As an example, hybrid and rotary types do not require a runway for takeoff and landing in contrast to the fixed wing types; however, their range is significantly lower compared to the latter ones. On the other hand, despite having a longer range compared to the rotary-type UAVs, fixed-wing UAVs lack agile maneuverability and are more vulnerable to stalls and incapable of sustaining flight at low speed (Townsend *et al.*, 2020). Due to operating at low to moderate Reynolds number flow regime, they are highly susceptible to flow separation, LSB (laminar separation bubble) formation, etc., which affects their flight performance and stability. To improve their flight

characteristics, owl-inspired leading-edge serrations are of great research interest due to their potential as a passive flow control device. It had been hypothesized that owls' leading-edge serrations alter the adjacent flow field to some extent in order to suppress the aerodynamic noise, impact its aerodynamic performance, and function as a passive flow control mechanism (Graham, 1934; Kroeger et al., 1972; Lilley, 1998; Wagner et al., 2017; Jaworski and Peake, 2020; Lawley et al., 2019; and Nafi et al., 2020). Noise generation during gliding flights of a Florida barred owl was investigated by Kroeger et al. (1972). They removed the leading-edge serrations from the owl's wing and recorded the noise spectrum; however, the results did not show any significant difference in the noise level compared to the noise data obtained from the unmodified wing. Wind tunnel tests on two prepared owl wings were also included in the scope of the work by Kroeger et al. (1972). The removal of leading-edge serrations prompted flow separation near the leading edge. They suggested that the serrations serve as "vortex" sheet generators (several angled plates that are usually attached to an aerodynamic surface to generate swirling flow behind them) that keep the flow attached over half of the wing surface from the leading edge. Geyer et al., (2017) conducted wind tunnel experiments on prepared barn owl wings and demonstrated that leading-edge serrations induced a slight increase in lift and a small decrease in noise during gliding flight. Also, in comparison, the clean wing without serrations had a strong noise source at the wing tip, which suggested that the leading-edge serrations might eliminate/ reduce wing tip noise. It is interesting that these serrations are only present in primary feathers, which form the leading edge of the distal part of the wing. To investigate their functionalities during gliding flights as well as noise reduction characteristics, Rao et al. (2017) conducted a combined study of numerical and experimental measurements on an idealized (flat plate) single feather model with straight slitted LE serrations. They showed that LE serrations could control laminar–turbulent transition on the suction side of the model at all angles of attack (AOA). They also observed that high-frequency noise was suppressed at 20° AOA and a slight drag reduction was achieved due to serrations at the leading edge. However, reduced aerodynamic performance was observed below 15° angle of attack for the serrated model. Based on the geometrical shape of the serrations, Klan et al. (2010) constructed an array of solid and flexible comb-like structures to investigate their influence on the flow field of a NACA airfoil at low angles of attack (0°, 3°, 6°) with the Reynolds number being 40 000, 60 000, and 120 000. Their PIV study results showed that the influence of leading-edge serrations depended on multiple factors (e.g., Reynolds number, angle of attack, flexibility, orientation of the combs in the spanwise direction, etc.). Also, in all the experiments, they observed that the size of the separation bubble was impacted due to the leading-edge serrations; however, the bubble always occurred at the leading edge. Winzen et al. (2014) conducted time-resolved PIV and force measurement studies using two types of cylindrical shaped serrations, using two different materials: metal and silicon. They were assembled on a barn owl wing model. The authors reported increase in drag coefficients with similar lift coefficients (compared to the smooth leading-edge case) for all the cases. They also observed that the length of the separation bubble was independent of the Reynolds number (40 000–120 000) effects when the metal serrations were used.

The aerodynamics characteristics of bio-inspired serrated wings' geometries, such as sawtooth patterns, wavy formations, sinusoidal

structures, and slitted designs, have been thoroughly studied (Jaworski and Peake, 2020). However, these investigations utilize simplified bio-inspired models rather than the precise geometry of serrations found on owls. This work focuses on owl wing serrations that are notably smaller than the wing's chord length and are oriented at an angle relative to the freestream. The influence of these microscale LE serrations on boundary layer, separation, and turbulence in the near wake remains open questions. The gap in the literature regarding this issue arises from the formidable challenge associated with numerically simulating the effects of these diminutive serrations, given their minuscule size and their abundance along the leading edge of the wing. Traditional wind tunnel experiments, whether conducted with preserved owl wings or live birds, provide valuable insights; however, they do not isolate the specific flow dynamics associated with individual wing features, such as LE serrations, trailing-edge fringes (TE), and velvety surfaces, among others. This holistic perspective is exemplified by the comprehensive wake field data discussed by Lawley et al. (2019).

The objective of our study is to illuminate the intricacies of flow dynamics attributed to the incorporation of "owl's leading-edge serrations" into an owl-airfoil-based wing. To capture the full spectrum of small-scale motions, we employ a direct numerical simulation (DNS) approach to resolve the flow-field dynamics across the range of scales. Most numerical research today on owl wings simplifies the airfoil by employing symmetric profiles, such as the NACA0012, while many studies turn to simplified, bio-inspired serrations, including sinusoidal, sawtooth, and similar patterns, to circumvent the complexities associated with meshing and solution convergence due to the intricate nature of actual serrations (Jaworski and Peake, 2020; Wang et al., 2019). Our approach utilizes the same size and shape as those found on actual owl wings, which were designed using data from the research conducted by Bachmann and Wagner (2011).

## II. METHODOLOGY

The airfoil used in this study is a generic owl airfoil (Liu et al., 2006), which was also used in the study by Beratlis et al. (2020) to simulate the flapping flight of an owl. This airfoil has also been utilized in the experimental study by Anyoji et al. (2018). The owl airfoil can be characterized by high camber and very low thickness near the trailing edge (see Fig. 1). Note that the surface of the owl wing is smooth in this study unlike a real owl wing, which is covered with elongated pennulae (velvety surface). The LE serrations have been modeled based on the data from the study by Bachmann and Wagner (2011). They estimated three-dimensional shape of the natural serrations of a Barn owl wing using confocal laser scanning microscopy. In this study, we utilize their first-order approximation to model the serration shapes and orientations along the leading edge of our model wing.

Owls have leading-edge serrations of different sizes and shapes, which vary across species; however, the larger species have larger serrations (Weger and Wagner, 2016). Also, the length of the serrations is not same across the span of a species (i.e., from the mid span to the wing tip). The average length of serrations for a Barn owl wing is 2.67 mm and the gap between two neighboring serrations is 0.57 mm, while the mean wing chord is approximately 17.1 cm (Bachman, 2010; Jaworski and Peake, 2020). Their flight Reynolds number also varies based on their flight speed (2.5–7.0 m/s) (Wagner et al., 2017), which results in flight Reynolds number varying between 40 000 and 120 000. From Kroeger et al. (1972) experimental study with natural owl wing [which was later revisited by Anderson (1973)], it was suggested that
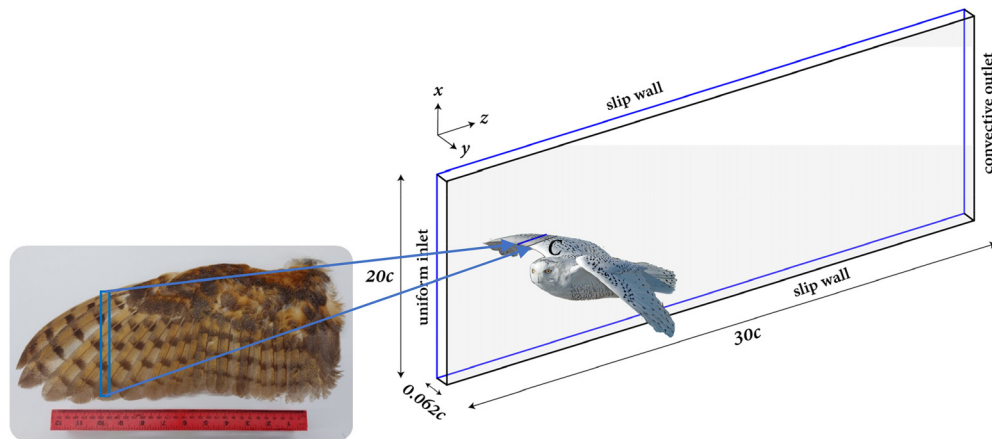
**FIG. 1.** Computational domain around a section of the owl wing. Here, c denotes to average chord length; z axis denotes to the streamwise direction, x axis is the cross-stream direction, while the spanwise direction is represented by y axis.

serrations are particularly effective at delaying stall as much as until 30° AOA. However, it should be noted that a natural owl wing has surface features (i.e., velvety down feathers), alula, slotted wingtip, etc., in addition to LE serrations, and these features could have additional effects on the flow downstream the leading edge. In this work, we focus on simulating serrations induced flow dynamics at 20° AOA at an intermediate Reynolds number (40 000) to assess the effectiveness of serrations in delaying stall (i.e., mitigating flow separation). Most of the airfoils have stall AOA ranging from 12° to 20° (Abbot *et al.*, 1945; Johnson, 2013) (i.e., for thin airfoils, large AOA causes flow separation starting from the leading edge of the wing, which may reattach near the trailing edge). Hence, we choose 20° AOA for our simulation so that stall phenomenon can be observed on both wings. In addition, the choice of Reynolds number is based on owl's flight Reynolds number, which ranges from 40 000 to 120 000. To minimize the computational cost, we simulate the flow around owl wing at 40 000 Reynolds numbers.

### A. Computational approach

The flow field around the owl wing is resolved using the DNS method. An IB (immersed boundary) formulation is utilized and the equations governing the dynamics of the flow are solved on a structured Cartesian grid where the requirement for the grid lines to conform to the airfoil is relaxed and boundary conditions are imposed using a direct forcing technique. This approach is a good fit for this class of problems as (i) it grid generation, especially for the case of the serrations and (ii) highly efficient structured solvers can be used, where mass, momentum, and turbulent kinetic energy (TKE) are conserved. Capuano *et al.* (2023) presented a cost-vs-accuracy study for three different solvers: the present IB solver, the spectral element solver Nek5000, and the finite-volume solver OpenFoam for the case of the flow around a sphere. They demonstrated that the cost efficiency of the IB solver is on par with the spectral element solver when first- and second-order moments are of interest.

The Navier–Stokes equations for incompressible flow are solved on a staggered Cartesian grid using a semi-implicit projection method for time advancement (Balaras, 2004). In the spanwise direction, all terms are treated implicitly to advance in time using a second-order Crank–Nicholson scheme in order to eliminate restriction to the time step, while all other terms are advanced explicitly using a third-order Runge–Kutta scheme. For spatial derivatives, second-order central difference scheme was used on a staggered grid setting. The pressure Poisson equation is solved using a generalized cyclic reduction algorithm preceded by spanwise fast Fourier transform (FFT) of the 3D Poisson equation (with periodic boundary condition in the spanwise direction), which produces a series of 2D Helmholtz equations in the wavenumber space (Yang, 2005). The code is parallelized using the domain decomposition technique and has been validated for numerous cases in a similar Reynolds number range as is adopted in this study, for example, flapping foils (Rahromostaqim *et al.*, 2016), rotating foils (Posa *et al.*, 2016; Posa and Balaras, 2018), and bluff bodies (Posa *et al.*, 2016; Pal *et al.*, 2017).

The computational domain around the owl wing is shown in Fig. 1. The governing equations are solved on a Cartesian grid of cuboid cells (fluid), while the owl wing surface (solid) is immersed in it. The owl wing surface is described via a Lagrangian grid consisting of triangular cells, which is not aligned with the Cartesian grid. Boundary condition is introduced in the fluid–solid interface using an immersed boundary formulation proposed by Balaras (2004) and Yang and Balaras (2006). The overall method can be summarized as follows: the Cartesian grid is categorized into three types of node points based on the relative location of the triangular mesh over the owl wing surface via a ray tracing technique (see Beratlis *et al.*, 2020; Smith *et al.*, 2010). Nodes inside the owl wing are tagged as "body points," while nodes outside the owl wing with at least one neighboring body point are tagged as "forcing points," and all other nodes across the Cartesian grid are tagged as "fluid points." The velocity field is then reconstructed on the forcing points using linear interpolation to implement the no-slip boundary condition. Also, a convective boundary condition is used in the outflow plane, which allows the fluid to exit the domain without distorting the flow inside the domain (Orlanski, 1976), while the slip wall refers to a frictionless surface (zero-wall normal velocity as well as the normal gradients of the velocity components parallel to the wall).

Two cases have been investigated in this setup: with and without serrations. The computational domain extends to 20c in the downstream direction from the mid-chord and 10c in the upstream direction. The vertical extent of the domain is 20c, while the spanwise length is 0.062c. The gap between serrations is very small, which necessitates high-grid resolutions in the spanwise direction; as a result, the spanwise extent is chosen to enclose 11 serrations resulting in 0.062c spanwise extent to reduce the computational cost. The grid resolution is $1141 \times 402 \times 1202$ in this study, which is based on the grid convergence study by Beratlis et al. (2020). For example, spatial resolution near the wing surface is 0.0015c in the streamwise direction and 0.00055c in the cross-stream direction. For the cells neighboring the serrations, both streamwise and cross-stream grid resolutions are 0.0005c. The CFL (Courant–Friedrichs–Lewy) number is set to a constant value of 1.1, resulting in time steps in the range of $0.4 \times 10^{-3}$. We should note that for this particular configuration, there are no experimental results for validation. We used a prior study on Eppler foils at similar AOA and Re (see Posa et al., 2017) as guideline to design the grid especially in the near wake region. Posa et al. (2017) compared the results to the experiments by Spedding and Mcarthur (2010) with excellent agreement.

In this computational setup, the grid resolution in the spanwise direction is capable of capturing three dimensionalities with some limitations (such as ineffectiveness of capturing the formation of the large stall cells due to limited spanwise domain size) (Taira and Colonius, 2009). Unlike experimental studies, where end plates (flat plate perpendicularly mounted at the tip of the wing and aligned parallelly with the freestream to obstruct the spanwise flow, preventing formation of tip vortex) are used to improve mean spanwise uniformities (although vortex shedding frequency does not get affected when aspect ratio, $AR \geq 7c \times \sin(AOA)$, where $AR = \text{span/chord}$, see Boutilier and Yarusevych, 2012), numerical simulations utilize periodic boundary conditions to simulate an infinite medium in the spanwise direction. Such practices are to reduce the computational costs and require large spanwise domain so that the stochasticity of the fully developed turbulent flow in the spanwise direction can be ensured. Hence, the best practice among the researchers is to adopt a spanwise domain length of 0.5c for high AOA cases (massive flow separations) and 0.2c for low AOA cases (Eisenbach and Friedrich, 2007; Kitsios et al., 2011; Breuer and Jovicic, 2001a; Hoarau et al., 2003; and Zhang and Samtaney, 2016). It is apparent that the spanwise domain extent is not large enough in our case to meet the aforementioned criterion, particularly large-scale 3D flow structures such as stall cells cannot be captured. Hence, this study can be considered as a quasi-3D solution for the current fluid flow problem rather than being capable of fully capturing all 3D flow phenomena. Zhang and Samtaney (2016) studied the effects of spanwise $AR$ extensively using DNS at 50 000 Reynold numbers. According to their findings, minimal effects were observed on the mean aerodynamic quantities (mean location of separation and reattachment as well) due to the $AR$ variation; however, turbulent quantities (i.e., Reynolds stress components, budget terms, etc.) were mostly overpredicted in the case of small aspect ratios ($AR$). Since our study mainly focuses on the comparison of flow physics between the serrated and the smooth leading-edge wing, it will provide insights on the qualitative aspects of the current fluid flow problem despite the limitations with the spanwise extent of the computational domain. Hence, the effects associated with limited span are present in both cases; however,

the only variable being the serrations will highlight the alteration of flow physics in a qualitative manner.

In the current work, x, y, and z denote to cross-stream, spanwise, and streamwise directions, respectively. Similarly, w, u, and v are the velocity components. All the results shown in Secs. III A–III C have been normalized for ease of comparative analyses.

## III. RESULTS

The organization of the result section is as follows: Time-averaged quantities are discussed in Sec. III A to elucidate the impacts of serrations on surface integral quantities as well as the mean flow pattern. Unsteady effects of serrations on the flow field are briefly discussed in Sec. III B, while its impacts on turbulence are detailed in Sec. III C. Finally, concluding remarks are presented in Sec. IV.

### A. Time-averaged characteristics

Time-averaged lift and drag coefficients are shown in Table I. From the differences between the two cases, we can remark that the footprint of owls' LE serrations on aerodynamic performance is not pronounced even at this AOA. A decrease of aerodynamic performance (by 3.2%) can be observed due to serration; however, production of lift is increased by 2% along with the increase in drag by 5.4%. We have also calculated the skin friction coefficient and the pressure coefficient along the wing surface (see Fig. 2) in order to obtain the spatial distribution of the aerodynamic loads on the wings to look for discrepancies, if exist. As the lift coefficient over a wing surface is derived from pressure coefficients (i.e., surface integral of pressure coefficients) (Torenbeek et al., 2009), we present pressure coefficient distribution over the wing surface to compare with time-averaged flow patterns.

Figures 2(a) (serrated case) and 2(b) (smooth case) depict the surface contours of time-averaged skin friction coefficient ($\overline{C_f}$), whereas the $\overline{C_f}$ profile comparison is shown in Fig. 3(b). In Fig. 3, the coefficients are extracted from the slice (location indicated with black line over the wing) shown in Fig. 3(a). Black contour lines on the wings' surfaces in Figs. 2(a) and 2(b) denote to $\overline{C_f} = 0$ (zero-crossings). Comparing the two cases, the skin friction profiles as well as the pressure coefficients [$\overline{C_p}$, Fig. 3(c)] of the lower surfaces are identical since the serration does not appear to impact the lower surface flow at this AOA. However, the upper surface embodies the effects of modified profiles induced by serrations at the leading edge.

It is evident from the upper surface $\overline{C_f}$ profile [Fig. 3(b)] that the flow separates at the leading edge (zone of negative $\overline{C_f}$) and then reattaches close to the leading edge for both cases (0.05 z/c for smooth wing and 0.08 for serrated wing). The $\overline{C_p}$ profiles in this region (0–0.05 z/c for smooth, 0–0.08 z/c for serration) show nearly constant profile (pressure plateau), which, after reattachment, has a steeper negative gradient for the serrated case. The regions of favorable (negative

**TABLE I.** Comparison between aerodynamic force coefficients and dominant frequencies at different AOAs.

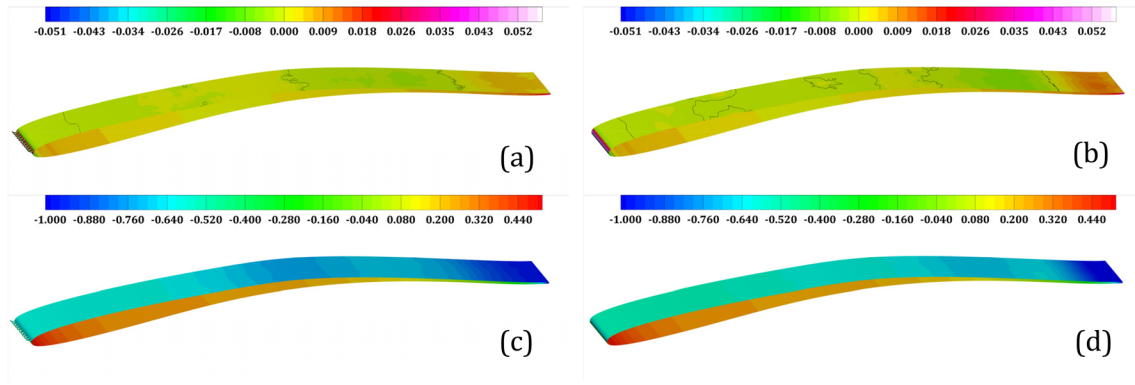| Case | Angle of attack | Time-averaged $C_L$ | Time-averaged $C_D$ | $\dfrac{C_L}{C_D}$ | $St = \dfrac{fc}{U_\infty}$ |
|---|---|---|---|---|---|
| Serration | 20° | 1.56 | 0.58 | 2.69 | 0.2375 |
| Smooth | 20° | 1.53 | 0.55 | 2.78 | 0.2 |

**FIG. 2.** Contour plots of time-averaged skin friction coefficient, $\overline{C_f}$: (a) serration (b) smooth; time-averaged pressure coefficient, $\overline{C_p}$: (c) serration (d) smooth.

pressure gradient) and adverse pressure gradients (APG) (positive pressure gradient) can reflect the location of secondary vortices, which will be shown in Secs. III B and III C. From the $\overline{C_f}$ profile of the serrated case, sustained reattached flow is observed from 0.08 z/c to 0.5 z/c, while the smooth wing depicts scattered zones of reattached flow within this separated region, which can be referred to secondary separation (Jones *et al.*, 2008). Near the trailing edge, the difference is more prominent as the reattached zone is significantly larger for the serrated wing, which is also evident from the favorable pressure gradient at this region [Fig. 3(b)]. The magnitude of $\overline{C_p}$ is larger for the serrated case (over almost entire upper surface) compared to the smooth wing, which explains higher drag force production as an airfoil at high AOA can be considered as a bluff body and the main drag component will be form drag in that case (Buresti, 2000; Swalwell *et al.*, 2003).

The $\overline{C_f}$ profile over the LSB location has a common shape for airfoils, which generally contains a pronounced negative $\overline{C_f}$ peak that indicates transition point (Jones *et al.*, 2008; Klose *et al.*, 2021). In our case, we observe this peak right at the leading edge (0.0 z/c) in Fig. 3(b)

for both cases, which means that the transition point coincides with the separation point. This is also evident from the Reynolds stress, turbulent kinetic energy, etc., which will be shown in Sec. III C.

The main flow features associated with the surface contours of $\overline{C_p}$ can be visualized from time- and spanwise-averaged streamwise velocity ($\langle \overline{w}/U_\infty \rangle$) contours and streamlines colored with velocity magnitudes shown in Fig. 4. The vortex shedding frequencies for both cases (Table I; $St \sim 0.2$) are similar to bluff body-like shedding characteristics (Zaman *et al.*, 1989; Yarusevych *et al.*, 2009) of the flow, which originates from the leading-edge separation bubble and so-called trailing-edge vortex, and influenced by their interactions (Huang *et al.*, 2001). Note that there is no universal definition for the term vortex (Jeong and Hussain, 1995), but it is generally accepted that a vortex will have a spiraling/closed-loop instantaneous streamline pattern with the vortex core having the most concentrated vorticity (Robinson, 1991; Chakraborty *et al.*, 2005). Mean location of both the separation bubble/vortex (SV) and TEV can be observed in Fig. 4 for both cases; however, the differences lie in topology, (i.e., size), velocity profiles (i.e., reverse flow intensity), and other secondary features (i.e.,
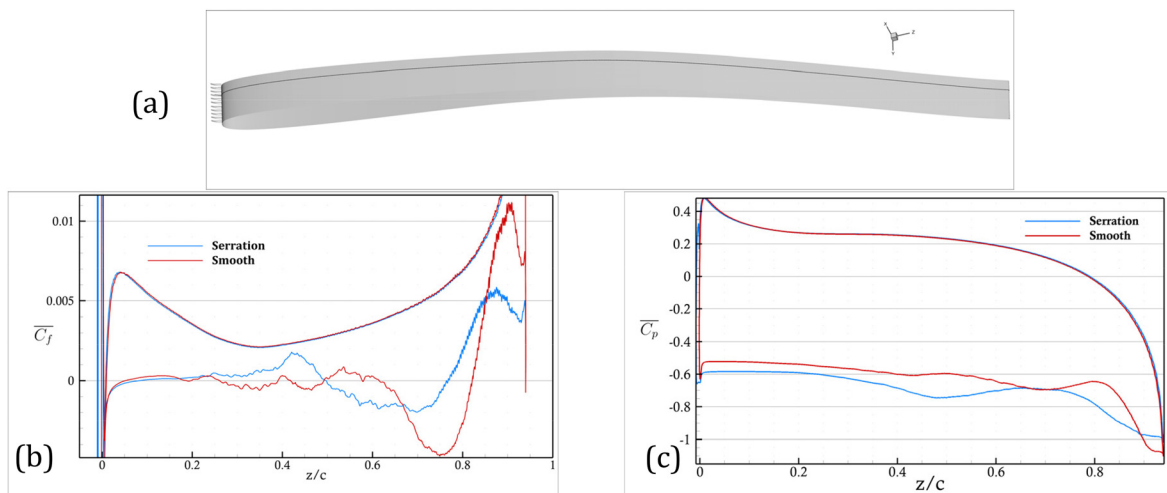
**FIG. 3.** Comparison of (b) time-averaged skin friction coefficient, $\overline{C_f}$, and (c) time-averaged pressure coefficient, $\overline{C_p}$. For both cases, the coefficients were taken from a slice (black line) shown in (a). The x axis represents normalized streamwise locations (z/c).
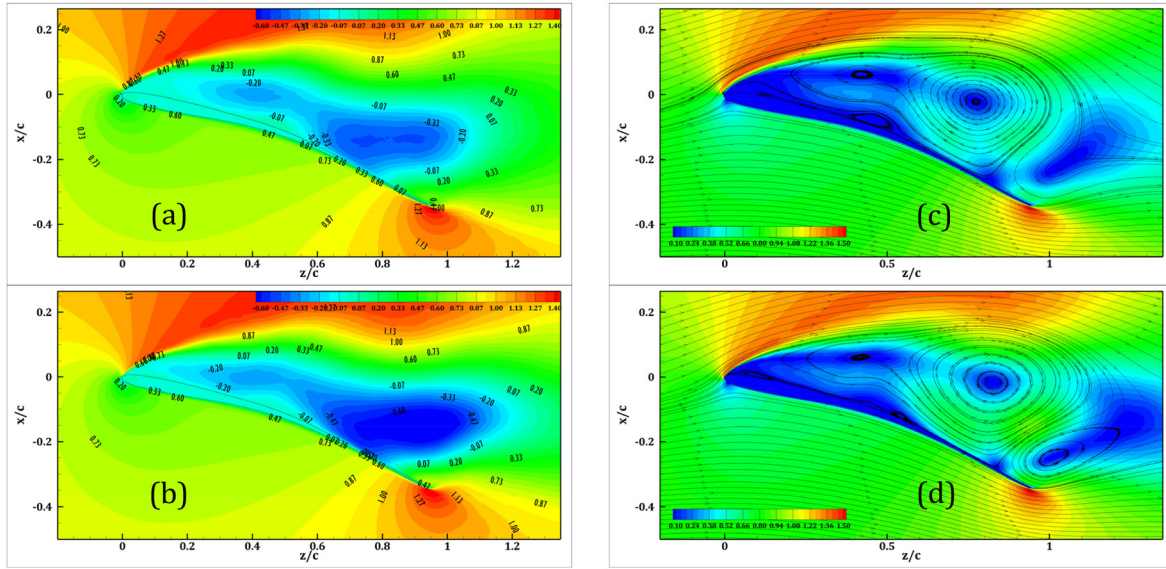
**FIG. 4.** Time- and spanwise-averaged streamwise velocity, $\langle \overline{w}/U_\infty \rangle$ for (a) serration, (b) smooth case; streamlines from time- and spanwise-averaged velocity field for (c) serration, (d) smooth case shown over velocity magnitude contour plot.

transition location, secondary bubbles, etc.). In regard to the size of the separation bubble, smooth wing's upper surface depicts a bigger one in comparison with the serrated case. The velocity profiles inside the bubble show much stronger recirculation region for the smooth wing as

shown in Fig. 5 (S4–S9) based on time- and spanwise-averaged streamwise ($\langle \overline{w}/U_\infty \rangle$) velocity profiles. The profiles are taken at several surface normal locations marked as S# shown in Fig. 5(a). From $\overline{C_f}$ profiles [Fig. 3(a)] and velocity profiles, we can see that the flow is
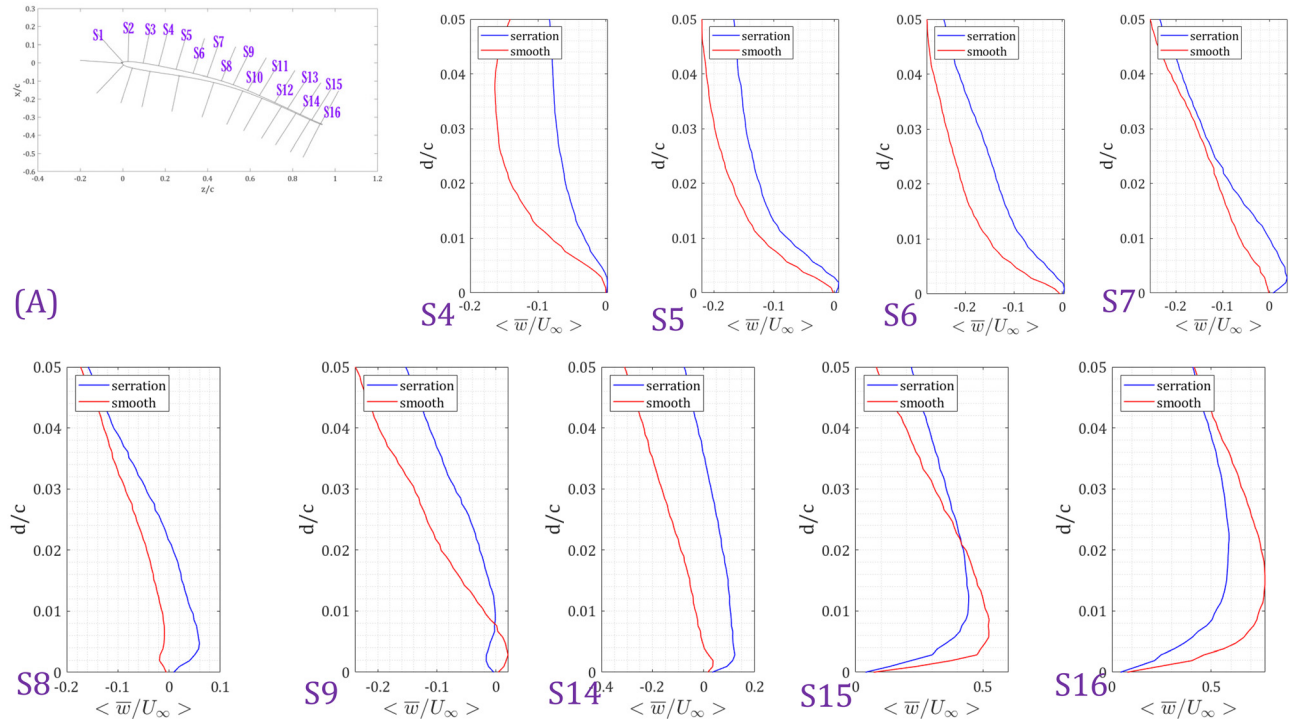


**FIG. 5.** Wall normal distance (d/c) vs time- and spanwise-averaged streamwise velocity profiles ($\langle \overline{w} \rangle/U_\infty$) over serrated and smooth wing's upper surface (S4–S16). Locations of the profiles over the upper surface are shown in (a).

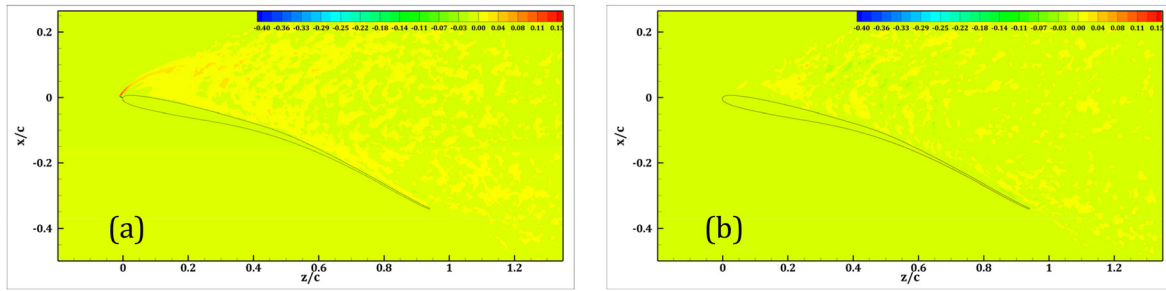**FIG. 6.** Time- and spanwise-averaged spanwise velocity, $\langle \overline{v}/U_\infty \rangle$ for (a) serrated, (b) smooth case.

attached near trailing edge for both cases; however, the TEV, which usually forms due to the shear layer roll-up from the lower surface of the airfoil (Huang *et al.*, 2001), appears to be weaker (Fig. 5: S15, S16) in the case of serration. In addition, the streamlines do not exhibit counterclockwise rotation loop in that region despite having a low-velocity vortex core region. This "half saddle" pattern may appear due to leading-edge vortex residing longer in that region than the TEV (Perry and Steiner, 1987). In Figs. 2(c) and 2(d), surface contours of $\overline{C_p}$ show a noticeable difference at the middle of the wings where the serrated case has a larger region of low-pressure zone compared to the smooth case. This is due to the presence of a secondary vortex in these locations, which can be observed in Figs. 4(c) and 4(d). The serrated wing features a larger vortex in this region compared to the smooth case (Fig. 5, S7 and S8); however, their direction of rotation is the opposite: CCW for serration and CW for smooth case; hence, only the serrated wing shows an attached flow.

Figure 6 exhibits time- and spanwise-averaged spanwise velocity ($\langle \overline{v}/U_\infty \rangle$) iso-contours. We observe that serration promotes enhanced spanwise momentum transfer in the immediate downstream vicinity of the serrations. This feature of the flow may be associated with facilitation of LEV stabilization during flapping flight. To stabilize LEV, root-to-tip spanwise flow is required as it contributes to the spanwise advection of vorticity that balances the production of vorticity at the leading edge (Jardin and David, 2014; Ben-Gida *et al.*, 2020). Also, spanwise flow facilitates smooth merging of leading-edge and tip vortex flows (Linehan and Mohseni, 2020). Over the entire upper surface, significant increase in spanwise momentum transfer can be observed for the serrated wing, especially near the wall, which also signifies increased three-dimensionality in the near-wall turbulence (Busse *et al.*, 2015; Huai *et al.*, 2015). Note that the spanwise flow development near LE was also observed in the experimental studies (with real owl wing) conducted by Kroeger *et al.* (1972) and Geyer *et al.* (2017).

At 20° angle of attack, vortex shedding due to flow separation introduces lift force oscillations on the both wings. The oscillation frequencies are shown in the lift coefficients spectra in Fig. 7 for both the serrated and the smooth wing. The highest energy containing peak is generally associated with the vortex shedding for lifting surface at high angles of attack, whereas the other dominant frequencies/harmonics are generally associated with periodic merging of rollup vortices, bubble bursting, and small-scale vortices impinging on the upper wing surface, etc. (Yarusevych and Boutilier, 2011; Nedic and Vassilicos, 2015; Huang *et al.*, 2001; and Chang *et al.*, 2022). In our case, St = 0.2 and St = 0.2375 are the vortex shedding/fundamental frequencies of the smooth wing and the serrated wing, respectively (Table I). Also, both

cases exhibit higher harmonics. For airfoils operating at high angles of attack and low Reynolds numbers, the higher harmonics are generally due to the effect of surface impingement of small-scale vortices generated from the interactions of large-scale vortices such as TE vortex/LE separation vortex (Chang *et al.*, 2022, Perez-Torro and Kim, 2017).

### B. Instantaneous flow dynamics

Spatial and temporal development of spanwise vortices is shown in Fig. 8. The figure depicts six different phases for both cases during a shedding cycle. The subfigures are sequenced based on the initiation of TEV formation (Fig. 8, t = 0) on the upper surface of the wing. It can be observed that there is a phase difference between the two cases. From t = 0 and t = Ts/5 (t = 5 as well), we can see that smooth wing develops TEV over the upper surface when the shedded TEV is located further away from the trailing edge compared to the serrated wing. Based on the formation and development of TEV as well as the separation vortex, the whole process for these two cases can be generalized: shear layer generated from leading-edge flow separation rolls up and merges, forming a large CW rotating separation vortex; CCW vortex is also generated at the trailing edge from the rollup of lower and upper surface shear layers. After the shedding event of a TEV, the CW separation vortex grows larger over time (vorticity is fed from the LE shear
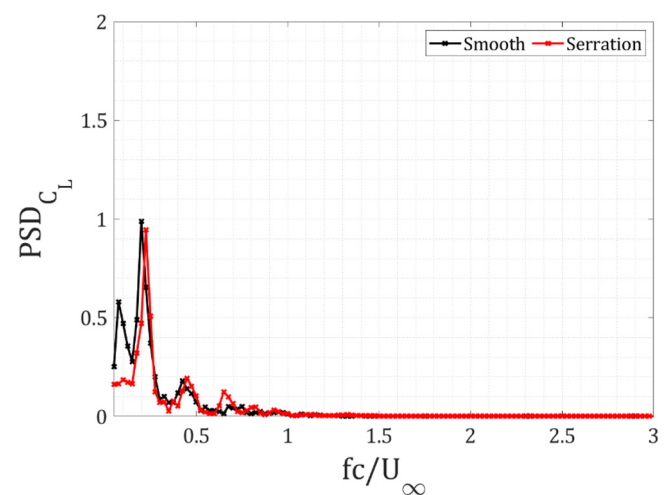


**FIG. 7.** Frequency spectrum of the lift coefficients ($C_L$). PSD abbreviates to power spectral density.
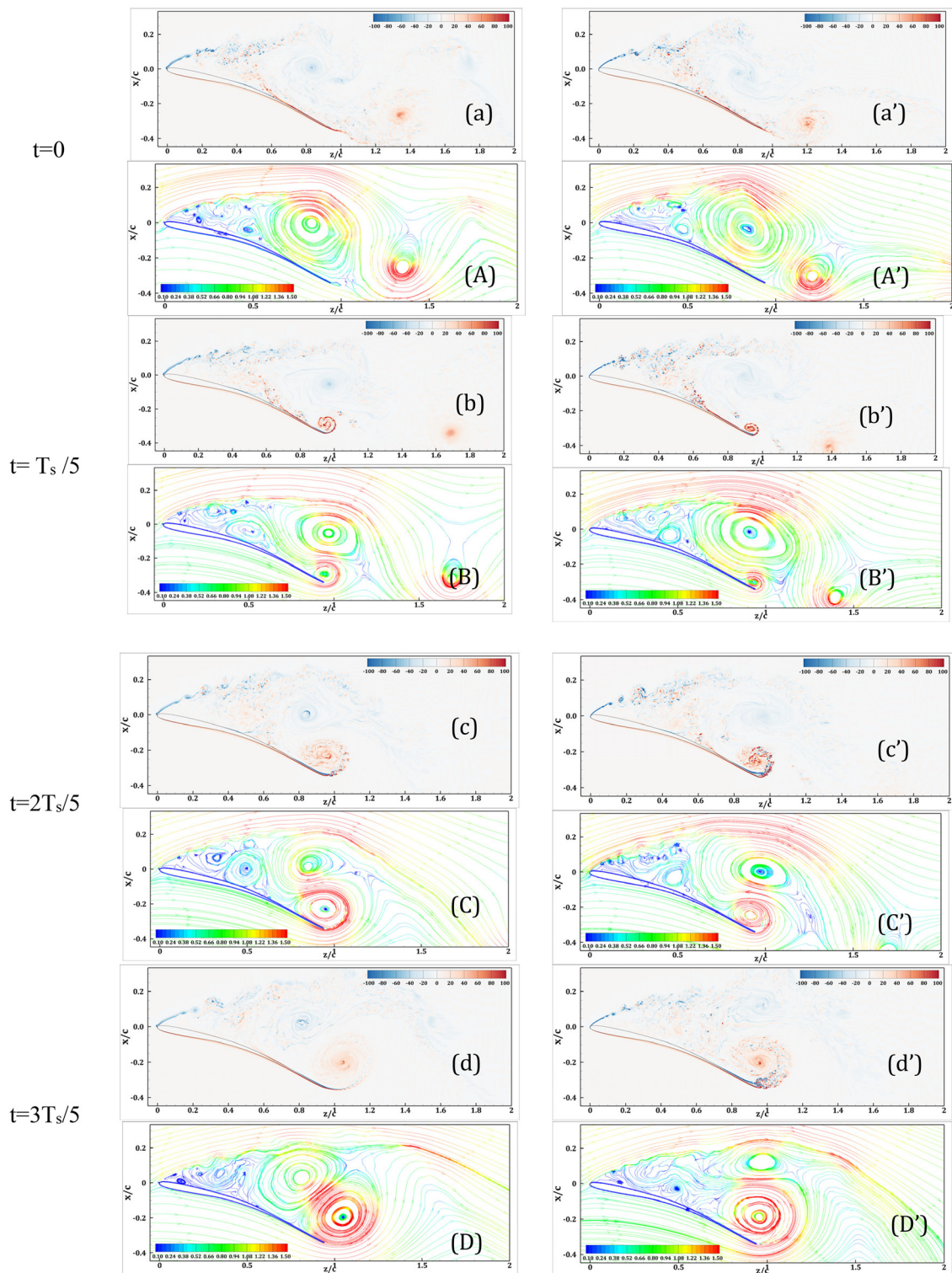
**FIG. 8.** Evolution of spanwise vorticity, $\omega_y c/U_\infty$ during one shedding period, $T_s$; (a)–(f) illustrates $\omega_y c/U_\infty$ of the serrated wing (left), while (a')–(f') denote to $\omega_y$ of the smooth case (right). (A)–(F)/(A')–(F') shows instantaneous streamlines colored with velocity magnitudes during each shedding phase shown in the spanwise vorticity contours. Time interval between two consecutive subfigures is $T_s/5$.
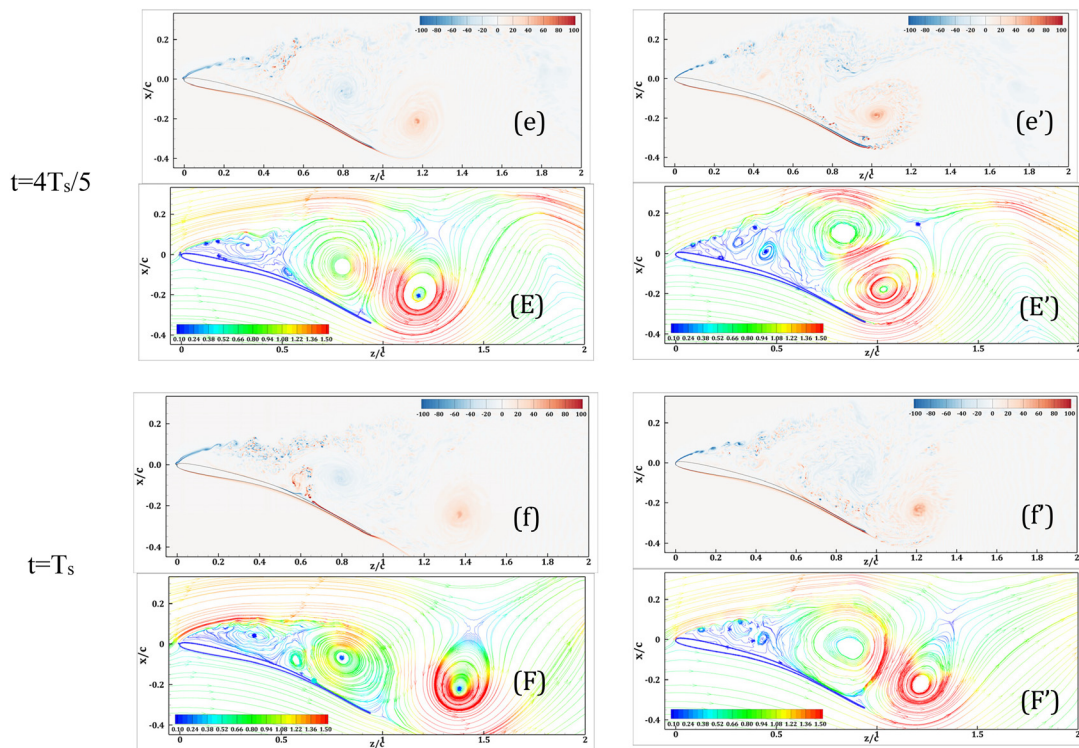
**FIG. 8.** (*Continued.*)

layer roller vortices), interacts with the other secondary vortex/vortices over the airfoil surface, and eventually covers almost half of the aftward portion of the airfoil (Fig. 8, t = 0). Afterward, a new TEV forms again; as it gets bigger in size and strength, it stretches the CW separation vortex, eventually splitting some of its vorticity into the wake which is convected downstream. Meanwhile, the growing TEV entrains fluid from the wake as evident by the saddle point (Cantwell and Coles, 1983), transport it toward the other secondary vortices located at the mid-chord of the airfoil. Eventually, when the TEV grows in size and strength to a certain extent, it gets detached from the upper surface and is convected downstream. The general flow patterns shown in our study for this airfoil at high AOA is in close agreement with the study by Breuer and Jovivic (2001a) and Lam (1996). However, some differences exist, especially, over the middle portion of the airfoil where interaction of TEV and separation vortex with the secondary vortices takes place.

The shedding characteristics of the flow over an airfoil at high AOA are mainly dependent on the interplay between the two large counter-rotating vortices (Breuer and Jovivic, 2001a; Lam, 1996). As a result of the interactions, the strength and size of the two shed vortices at the wake do not remain the same unlike the classical bluff body vortex shedding where symmetric wake is observed and vortices of equal size and strength persist downstream the flow. Hence, airfoil and flat plate at high incidence may produce asymmetric wake containing vortices of unequal strength (Breuer and Jovičić, 2001a; 2001b; Lam, 1996; and Freymuth et al., 1984), which has also been observed in our study as evident from the instantaneous streamlines and vorticity shown in

Fig. 8 where the shedded TEV is the stronger one, while the shedded CW vorticity is negligible (for both the cases).

From Figs. 8(c′) and 8(d′), t = 2$T_s$/5, 3$T_s$/5, we can observe that near the TE, flow separation occurs for the smooth wing during the TEV expansion period, while the serrated case shows attached flow at that region. Both cases illustrate the so-called "eruption phenomena" when separation vortex is close to the no slip wall (after the shedding of TEV) and subjected to intense viscous action. As a result, wall layer vorticity ejection occurs and secondary vortices form near the wall (t = 0, $T_s$/5, 2$T_s$/5) (Luton et al., 1995; Balci et al., 2015). This process is regenerative and feeds vorticity to the regions upstream. When the Reynolds number is more than 5000, this process generates a whole sequence of vortical structures to be ejected from the boundary layer (Kudela and Malecha, 2009). The formation of CCW vortex near the wall (∼0.5 z/c) is also owing to this phenomenon, which causes area reduction of the recirculation zone.

The main differences that can be observed from the instantaneous figures that the eruption phenomena produce secondary vortices at the middle of the wings that appear to be of different sizes (also evident from time-averaged contours in Fig. 4) as well as the turbulent boundary layer (TBL) at TE separates for the smooth case during the TEV enlargement period. The differences point toward wall layer vorticity eruption via (1) separation vortex as the eruption phenomenon depends on its strength, while it is near the wall (i.e., pressure gradient at the wall under the vortex) and viscosity (Kudela and Malecha, 2009; Doligalski et al., 1994); TBL separation during TEV enlargement phase (smooth wing) due to (2) complex trailing-edge vortex dynamics

generates APG near trailing edge. To determine the intensity of the vortical structures during these phenomena, we analyze the instantaneous flow fields' vorticity magnitude profiles during the aforementioned phases, which are shown at Fig. 9.

In Fig. 9(a″) (t = 0), the vorticity magnitude profiles are plotted to compare the local strength of the vorticity over the airfoil surface. The other two rows of sub-figures (t = 2$T_s$/5, 3$T_s$/5) shows the vorticity magnitude during the TEV expansion phases as shown in Fig. 8. From all subfigures of Fig. 9, we can observe that the core region of the separation vortex (SV) appears to be stronger for the serrated wing. Here, we adopt the vortex center definition provided by Strawn *et al.* (1999), which is the local maxima of vorticity magnitude inside a rotational region of the flow. It is also evident from the profiles shown in Fig. 9(a″) where the peak vorticity of the serrated wing's SV is higher in terms of magnitude. Similar trend can be observed regarding the TEV intensity when the smooth case is considered. During the expansion of TEV, smooth case depicts a significantly stronger TEV at the trailing edge as shown in the profiles [Figs. 9(b″) and 9(c″)]. A stronger SV will promote more vorticity ejection from the wall, as a result, the secondary CCW vortex formation would also be intensified accompanied by a strength reduction of SV, while it is near the surface (Luton *et al.*, 1995). On the other hand, a stronger TEV will generate a stronger induced velocity field, which, in conjunction with the SV-induced velocity field, would determine the overall flow pattern. The TEV, being stronger than the SV during the enlargement phase (higher vorticity magnitude at the vortex core), draws in fluids from the wake as well as the bottom surface of the wing, transport it toward the region

where secondary vortices are located (Fig. 8, t = $T_s$/5, 2$T_s$/5, 3$T_s$/5). The SV undergoes more pronounced deformation than the TEV during the development of TEV as interaction between two unequal-strength counter-rotating vortices will cause weaker one to deform more than the stronger one due to unequal induced strain field; however, both vortices will experience deformation due to the mutual-induced strain field (So *et al.*, 2007). In our case, we see similar phenomenon for both wings where the weaker SV undergoes significant deformation (Fig. 8) compared to the stronger TEV during its enlargement phase. Also, smooth wing's trailing edge exhibits flow separation during this TEV enlargement phase, which is associated with the stronger TEV strength. The initial formation of TEV before shedding resembles that of a wing tip vortex formation where the bottom boundary layer (pressure side) rolls up over the upper surface (due to pressure difference between upper and lower surface of the wing). A strong tip-crossing flow from the pressure surface to the suction surface ensues flow separation from the suction surface boundary layer at the wingtip, forms secondary and tertiary vortices inside the tip vortex close to the tip (known as tip vortex system). It has been observed that during the early stage of tip vortex formation (over the wingtip of the frontal half of the wing) when the tip crossing flow is not strong enough, favorable APG persists resulting in lack of flow separation in the tip region (Giuni and Green, 2013; Duraisamy, 2005). Hence, TEV strength beyond a certain limit might contribute to APG development as vortices by nature will always change the pressure distribution over a solid surface due to viscous–inviscid interactions.
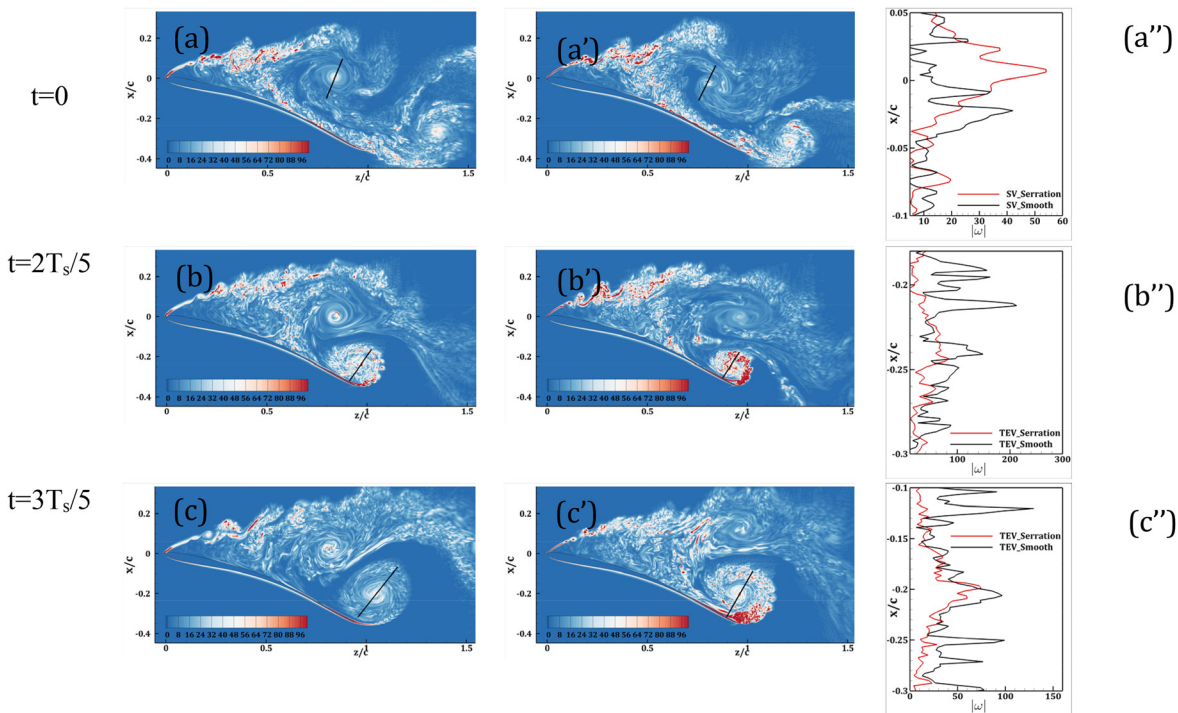


**FIG. 9.** Vorticity magnitude, |$\omega$| during t = 0, 2$T_s$/5 and 3$T_s$/5 instances shown in Fig. 8; (a)–(c) illustrates |$\omega$| of the serrated wing while (a′)–(c′) denotes to |$\omega$| of the smooth wing. Black lines illustrate the locations where vorticity magnitude data were extracted from. The lines were placed in such a manner so that they pass through the vortex cores and its boundaries. (a″)–(c″) are the line plots of the extracted vorticity magnitude data.
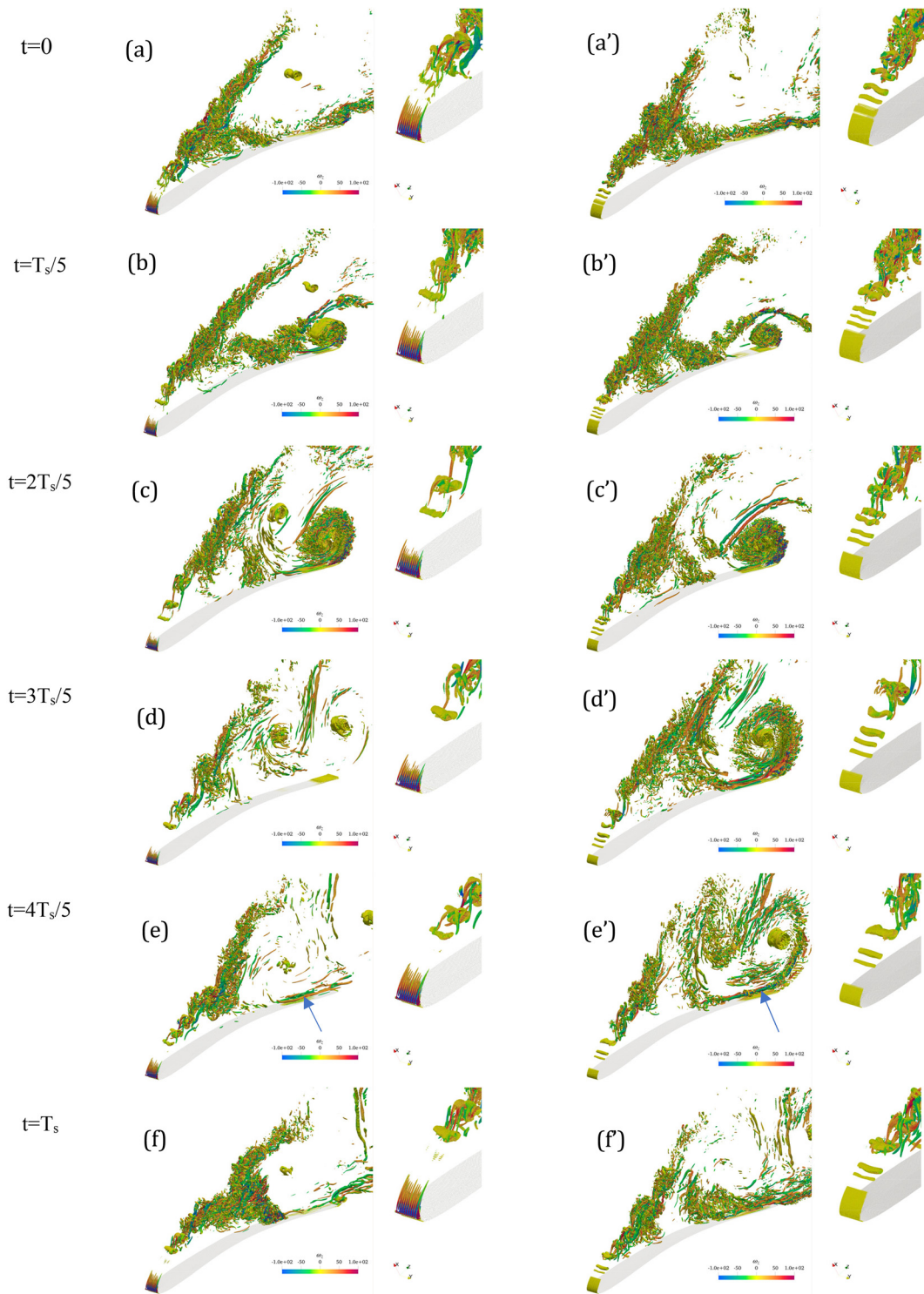
**FIG. 10.** Instantaneous iso-surface of Q-criterion ($Q = 1000$) colored with streamwise vorticity ($\omega_z c/U_\infty$), during the instances shown in Fig. 8; (a)–(f) illustrates the iso-surfaces over the serrated wing (left) while (a′)–(f′) shows the smooth case (right). Note that the left side of each individual figure [i.e., (a), (b), etc.] depicts the full wing, while the right side shows the magnified version near the LE for ease of visualization. The animation of iso-surfaces of Q-criterion during this shedding cycle is provided in supplementary file 1 (serrated wing) and 2 (smooth wing). Multimedia available online

Serrations are located upstream where the leading-edge flow separation initiates. As a result, the shear layer passes through the serrations. As they are angled and placed in a series across the span, their impacts on the three-dimensionality of the flow are significant. To observe the three-dimensional flow patterns around both wings, Q-criterion (second invariant of the velocity gradient tensor) values (Hunt *et al.*, 1988) are estimated to identify rotation-dominated regions in the flow. In Fig. 10, the iso-surface of the Q-criterion is presented during a shedding cycle as shown in Fig. 8. The iso-surfaces are colored with streamwise vorticity ($\omega_z c/U_\infty$). Both wings show dominant flow features: a shear layer generated from the flow separation at the leading edge rolls up into quasi-two-dimensional Kelvin–Helmholtz vortices (Yarusevysch *et al.*, 2008; Visbal, 2011; and Klose *et al.*, 2021) also known as KH rollers. In addition to the presence of large-scale structures such TEV and SV, we can also observe

an abundance of rib vortices in between the rollers. In the boundary layer near the trailing edge, a longitudinal vortex pair ($t = 4T_s/5$) can also be observed for both cases, which are known for their turbulent boundary layer thickening (when their common flow is away from the surface) and thinning (when their common flow is toward the surface) effects (Pauley and Eaton, 1988). These longitudinal vortices can occur naturally in TBL flows (can also be generated artificially) and significantly alter the dynamics of the boundary layer. Boundary layer thinning is associated with boundary layer separation prevention (via interaction of the vortex pair) but at the expense of enhanced skin friction drag (Pauley and Eaton, 1988), on the other hand, promoting BL thickening leads to flow separation. However, their effects are entirely dependent on how close/strong the vortex pairs are. As shown earlier in Fig. 8 ($t = T_s/5, 2T_s/5, 3T_s/5$), a serrated wing exhibits attached flow during the TEV enlargement phase. This can also be observed in the Q
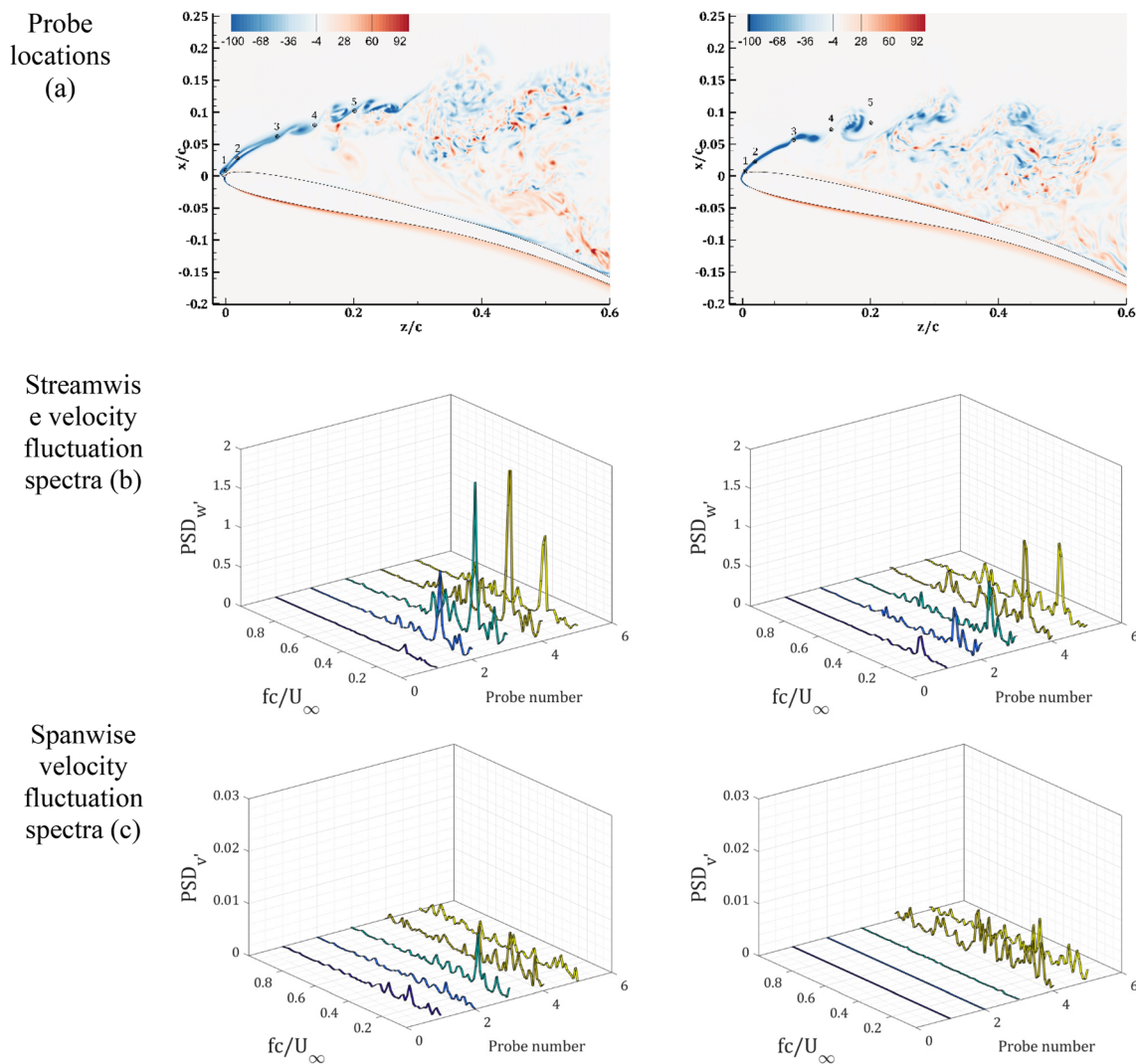


**FIG. 11.** Frequency spectra of the velocity fluctuations at the leading edge inside the separated shear layer; left: serrated wing, right: smooth wing. Probe locations are shown in row (a), frequency spectra of streamwise velocity fluctuations in row (b), and spanwise velocity fluctuations in row (c). PSD abbreviates to power spectral density.
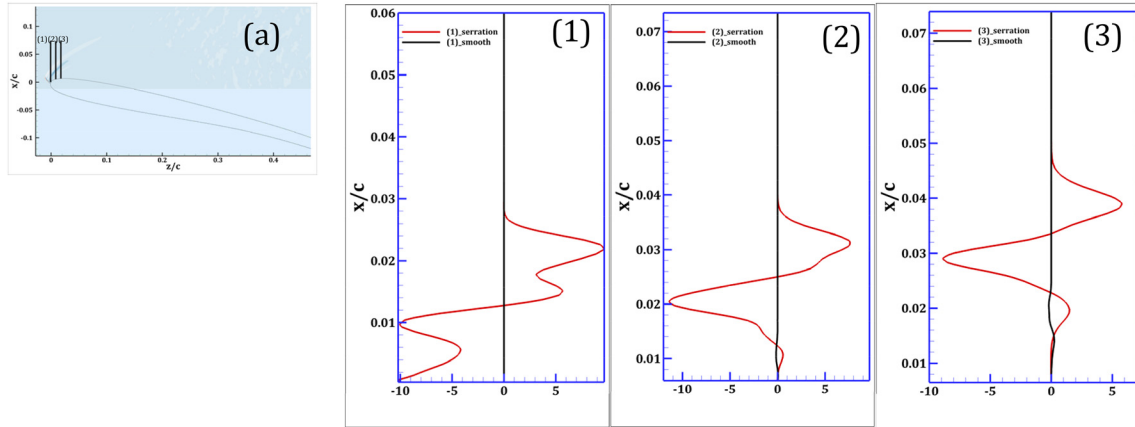
**FIG. 12.** Time- and spanwise-averaged streamwise gradient of spanwise velocity profiles (dv/dz); taken at three locations shown in (a) where location (1) is the leftmost location (closest to the LE), (2) is the location between (1) and (3), while location (3) is the rightmost. (1)–(3) depict the dv/dz profile at those aforementioned locations.

contours. TE surface of the serrated wing contains vortex pairs of "common flow up" (clockwise at the edge then anti-clockwise at the middle), whereas the smooth wing contains vortex pairs of "common flow down," which signifies TE BL thickening of the smooth wing [can also be observed in Fig. 8 (t = 2T$_s$/5, 3T$_s$/5)].

Typically, KH instability is the primary instability mechanism for flows involving laminar–turbulent transition with a separation bubble in the scope (Yang and Voke, 2001). Secondary instabilities may also be present in the vortex sheet (shear layer), which may coexist and coupled with the KH mechanism. Two such secondary instabilities have been reported often in literatures: one of them is two-dimensional subharmonic vortex pairing instability, which involves

pairing/merging of two KH rollers into one, whereas the other one is a three-dimensional instability associated with rib vortices formation, which undergo stretching in the streamwise direction and bend the core of the KH rollers (Metcalfe et al., 1987; Yang, 2013; and Zauner et al., 2019). In Fig. 11, frequency spectra of the streamwise and spanwise velocity fluctuations are shown for the temporal data of 20 shedding cycles, which were collected from the locations inside the shear layer [Fig. 11(a)]. The fundamental frequency (Table I) along with its harmonics can be observed at all probe locations in Fig. 11(b) for both cases. A noticeable difference between serration and smooth case can be observed in Fig. 11(c), where probes 1, 2, and 3 showing no distinguishable frequency peaks for smooth wing at this frequency range.
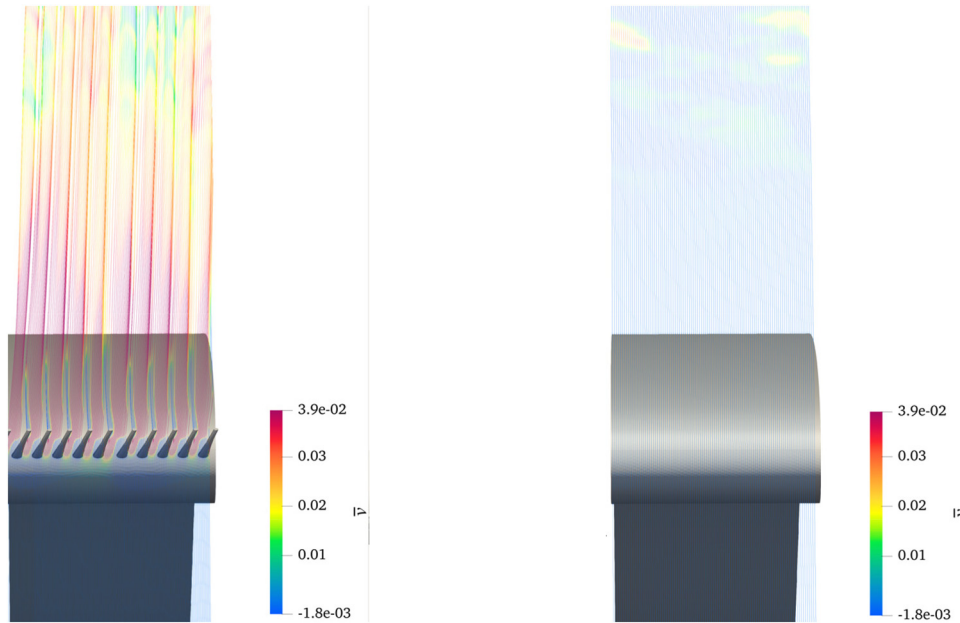


**FIG. 13.** 3D streamlines showing flow deflection effect by serrations. Streamlines colored with time-averaged spanwise velocity.

This indicates that three-dimensional perturbations emerge earlier when serration facing the freestream. As a result, early formation of rib vortices ensues (Fig. 10) (compared to the smooth case), which deforms the two-dimensional roller vortices. The shear layer eventually undergoes expansion through pairing/merging process of two neighboring quasi-two-dimensional rollup vortices as evident by the subharmonic of the fundamental frequency, which is found to be present in both spectra.

In Fig. 10, a notable difference exists between the two cases in terms of streamwise vorticity generation at the leading-edge shear layer. Serrated wing shows finite values, whereas the smooth case depicts null values close to where the leading-edge separation occurs. The origin of this streamwise vorticity generation can be traced back to streamwise gradient of the spanwise velocity (Bradshaw, 1987), which is shown in Fig. 12. The profiles are for time- and span-averaged quantity, which were extracted from the locations close to the leading edge shown in Fig. 12(a). From the mean vorticity equations, Bradshaw (1987) showed that "skewing" of spanwise vortex lines arises from streamwise gradient of the spanwise velocity, which means three dimensionalities in the flow originates from the flow deflection. Indeed, when the shear layer passes through the serrations, it deflects the flow toward the direction of the serration tip (see Fig. 13). Note



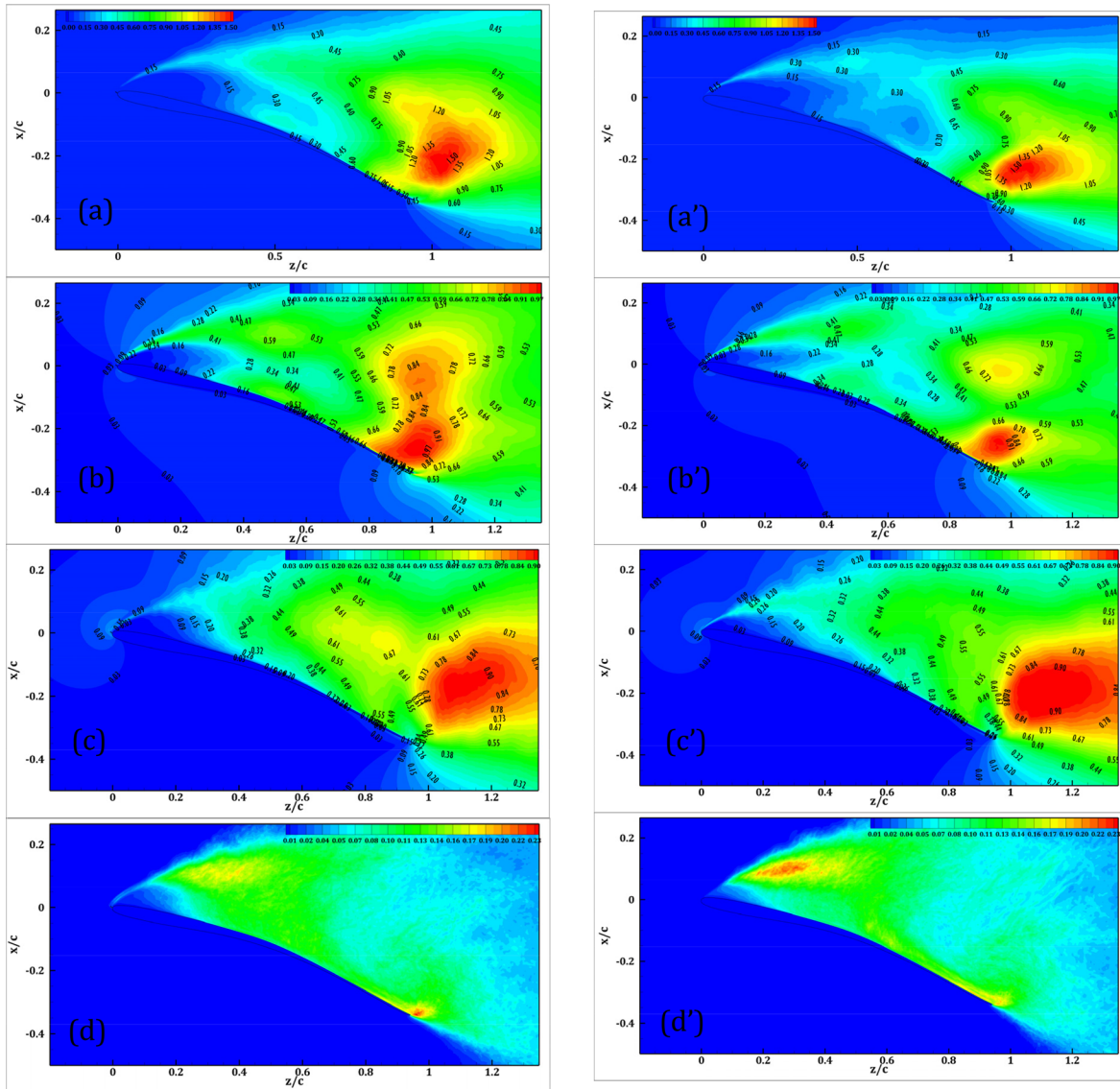**FIG. 14.** (a) Time- and spanwise-averaged turbulent kinetic energy (TKE) of serrated case, (a′) smooth case; RMS of streamwise velocity fluctuations for (b) serrated wing, (b′) smooth wing; RMS of vertical velocity fluctuations for (c) serrated wing (c′) smooth wing; RMS of spanwise velocity fluctuations for (d) serrated wing (d′) smooth wing. Note that TKE and RMS values are normalized by $U_\infty^2$ and $U_\infty$, respectively.

that negative gradients in Fig. 12 (1,2,3) refer to the location where foremost portion of the separation bubble is while the positive gradients are the location of the LE shear layer.

It can be observed from all subfigures of Figs. 8 and 10 that SV never shed completely from the upper surface of the wing; rather, it splits and parts of its vorticity is shed into the wake [also, see the animation showing iso-surfaces of Q-criterion during a shedding cycle in supplementary file 1 (serration) and 2 (smooth); multimedia available online]. SV is sustained by the instability mechanisms at the LE. Due to the subharmonic instability, two KH vortices will have different convective velocity (one will shift upward closer to the higher velocity side of the shear layer), which will eventually merge into a stronger one. During this merging process, abundance of small-scale turbulence is observed (McAuliffe and Yaras, 2009). Guha and Rahmani (2019) showed that turbulence intensity due to merging is dependent on the initial asymmetry of the KH billow shape (high initial asymmetry generates high turbulence during the merging). From the contour plot of the average TKE, we can see that serrated wing shows high TKE [Fig. 14(a)] in the downstream of the LE shear layer. Also, from visual inspection of the spanwise vorticity plots (Fig. 8), we can observe that the LE shear layer is of wavy shape starting from the location of

separation. Hence, we can surmise that serrations may intensify the vortex merging process, leading to enhanced momentum transport.

## C. Influence of serrations on turbulence: Statistical analysis

From the previous discussions, we showed serration-induced effects on the flow patterns. In this section, turbulent flow features around the wings are characterized. In Fig. 14, TKE (turbulent kinetic energy) and RMS (root mean square) of streamwise and spanwise velocity fluctuations are presented. As mentioned earlier, in our study, transition does not occur in a location over the separation bubble rather the flow is turbulent starting from the onset of separation. From the comparison between Figs. 14(a) and 14(a'), we can observe that TKE contour level is relatively higher in the frontal half of the serrated wing, especially at the mean location of the secondary vortices (see Fig. 4) over the upper surface (0.3–0.5 z/c) and its surroundings. This signifies stronger mixing between the high momentum fluid above the shear layer and low momentum fluid inside the bubble region. Both wings exhibit low TKE near the leading edge starting from 0 z/c to approximately 0.2 z/c. The fluid inside this region is relatively still (but
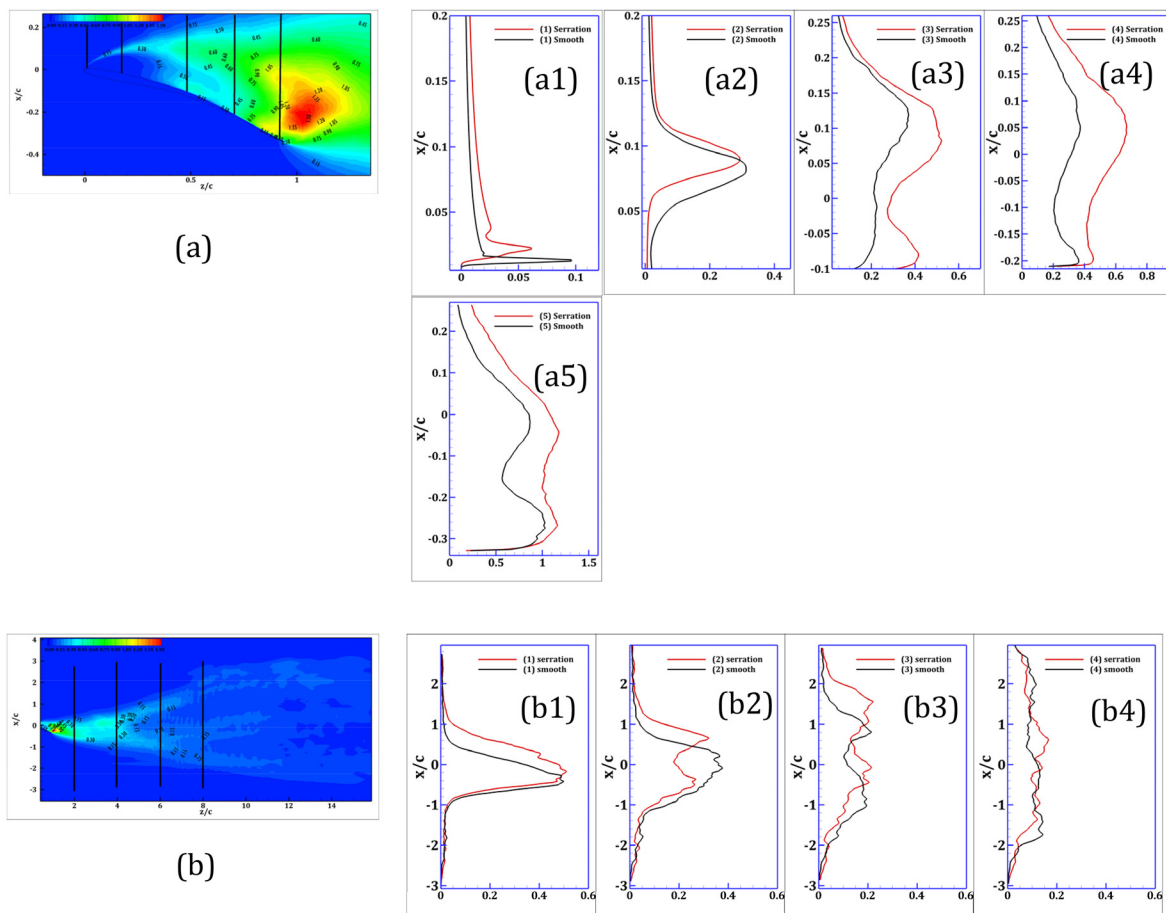


**FIG. 15.** Comparisons of TKE profiles. Data taken at the locations shown with black lines over the contour plot; (a) profiles over the wing (b) at the wake. Location numbering [i.e., (a1), (a2),…, (a5)] starts from the leftmost line in the contour maps in (a) and (b).

not completely stagnant, see Fig. 4), resembles that of a "dead air zone" inside an LSB; however, KH vortices and their interactions transport momentum in this region, which can be observed in Fig. 8 instantaneous streamlines. Interestingly, serrated wing depicts a larger zone of high TKE above the trailing edge compared to the smooth wing. This zone is where TEV and SV interact before the TEV being shedded into the wake; a larger zone of high TKE signifies SV and TKE (counter rotating vortex pairs) interactions promote a higher turbulent transport of momentum from the surrounding fluid. As a result, intensity of the reverse flow is reduced for the serrated wing.

From Fig. 15(a), it can be observed that TKE is higher in profile (a3)–(a5) for serration as can be seen in the contour plots in Fig. 14(a); however, near the LE shear layer [profile (a1)] peak value of TKE is higher for the smooth case, whereas in profile (a2), both of the profiles are very similar in terms of peak values. Although serrations exhibit a turbulence reduction feature in profile (a1), it is actually impacting the shear layer to develop 3D turbulence instead [see Fig. 16(a1)]. The streamwise, cross-stream, and spanwise velocity fluctuation profiles shown in Fig. 16 demonstrate that the peak RMS values of streamwise and cross-stream fluctuations are reduced, but spanwise fluctuations are non-zero unlike the smooth wing's shear layer. When the shear layer passes through the serrations at its early stage of development, serration impacts the flow in such a way that the extraction of turbulent energy from the mean flow is biased toward developing spanwise disturbances. The small bump seen in smooth wing's spanwise velocity fluctuation profile in Fig. 16(a1) is actually the foremost edge of the separation bubble. As the flow heads downstream [Figs. 16(a3)–16(a5)], all fluctuating components develop in both shear layers; however, serrated wing shows higher magnitudes of RMS fluctuations of streamwise and vertical velocities consistently. Regarding the spanwise fluctuations, the differences even out at the downstream zones of the contour [Figs. 16(a3)–16(a5)].

Also, serrated wing's shear layer is lifted up from the upper surface of the wing compared to the smooth case. This can be observed from TKE profiles as well as the RMS fluctuation profiles at (a1) location. This type of upward deflection of shear layer results in wake enlargement, which can be observed from Figs. 15(b1)–15(b4) profiles. Similar phenomenon has been observed in the study conducted by Al-Battal *et al.* (2016) where they conducted PIV experiments using NACA 0012 airfoil to investigate the effects of blowing on airfoil performance. They also observed a larger wake resulting from the upward deflection of the shear layer. From the wake profiles shown in Fig. 15(b), we can also observe that serrations do not have a strong effect on intensification of wake turbulence except larger wake is mainly developed at the near wake less than 7 chord length away from the wing.

Turbulent motions in the flow can generate additional momentum fluxes, and they can be interpreted as additional effective stresses known as Reynolds stresses, which comprises of normal stresses (diagonal terms of the Reynolds stress tensor) and shear stresses (off diagonal). In this section, Reynolds shear stress in the streamwise–vertical plane ($\langle u'w' \rangle / U_\infty^2$) is described, and the contour plot is shown in Fig. 17(top). The Reynolds shear stress is also used to indicate mean transition location in fluid flows where Reynolds stress reaches to 0.001 $U_\infty^2$ after the separation of the boundary layer (Ol *et al.*, 2005; Hain *et al.*, 2009). From the profile shown in Fig. 18(a1), Reynolds stress is already much higher at the shear layer close to the leading
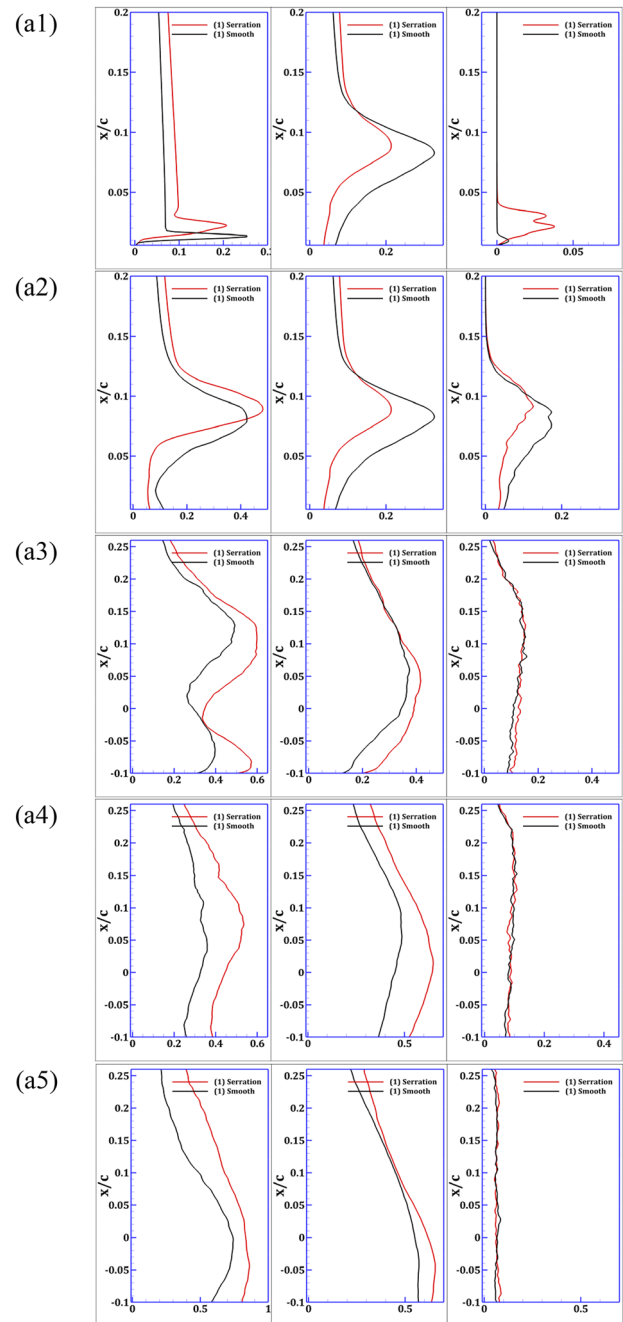


**FIG. 16.** From left: RMS of streamwise velocity fluctuations, RMS of cross-stream velocity fluctuations, RMS of spanwise velocity fluctuations at location (a1)–(a5) as shown in Fig. 15(a).

edge for both cases. As the shear layer heads downstream the flow, the sign of the Reynolds stress changes at 0.15 z/c for the smooth wing and 0.2 z/c for the serrated case [Figs. 17(a) and 17(a′)]. This can also be observed from Fig. 18(a2) that shear layer changes sign at a later location for the serration. To analyze the turbulent momentum

FIG. 17. Spanwise-averaged Reynolds stress $\langle\overline{u'w'}\rangle/U_\infty^2$ of (a) serrated wing (a') smooth wing; $\langle\overline{u'v'}\rangle/U_\infty^2$ of (b) serrated wing (b') smooth wing.

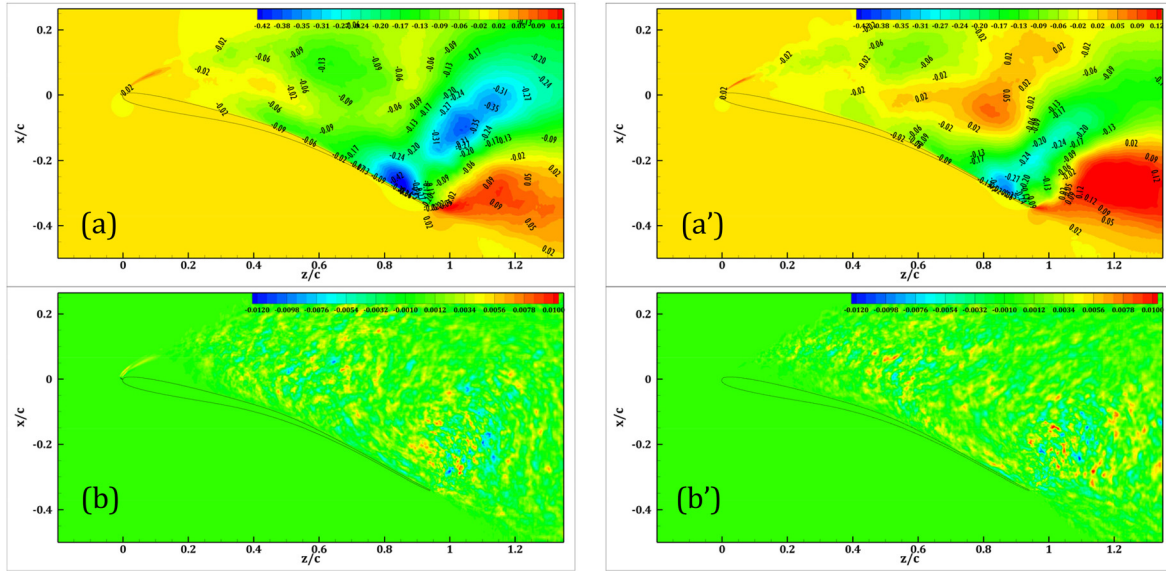transport in the flow, a similar approach to the quadrant analysis introduced by Wallace *et al.* (1972) can be employed. The time- and span-averaged Reynolds stress $\langle\overline{u'w'}\rangle/U_\infty^2$ is produced by four types of instantaneous events: Q2 $(+w, -u)$ and Q4 $(-w, +u)$ are associated with vertical turbulent momentum transport; Q2 is downward transport of high-speed fluid, Q4 is upward transport of low-speed fluid. On the other hand, Q1 is upward transport of high-speed fluid and Q3 is downward transport of low-speed fluid (Wallace, 2016; Soldati and

Banerjee, 1998). Hence, negative $\langle\overline{u'w'}\rangle$ creates gradient momentum flux, while positive $\langle\overline{u'w'}\rangle$ creates counter gradient flux (Wallace, 2016; Metcalfe *et al.*, 1987).

Near the leading edge, the serrated wing shows the smaller region of $\langle\overline{u'w'}\rangle \sim 0$, and this can also be observed in the TKE contour plots. At the TE, the serrated wing shows a large region of negative $\langle\overline{u'w'}\rangle$ (Q2 and Q4 types event dominant) compared to the smooth wing. This implies vertical turbulent momentum transport in that region is
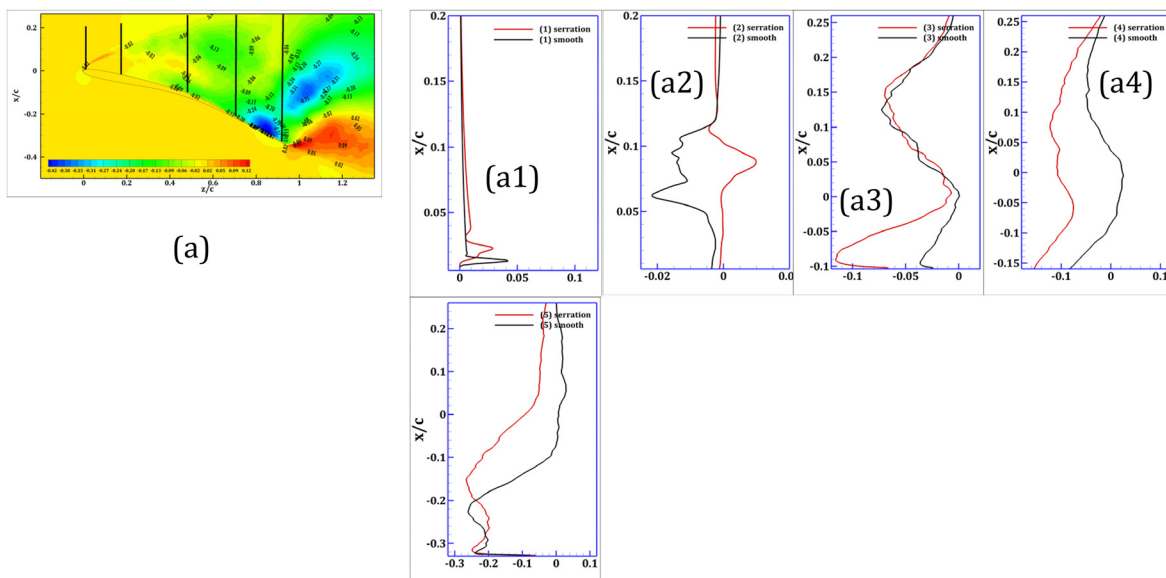
FIG. 18. Reynolds stress ($\langle\overline{u'w'}\rangle/U_\infty^2$) profile comparison. Data taken at the locations shown with black lines over the contour plot. Location numbering [i.e., (a1), (a2), ..., (a5)] starts from the leftmost line in the contour map (a).

quite significant. This zone is where TE and LEV interact mostly during the shedding cycle, bringing high-speed fluid from the surroundings. In time-averaged sense, the serrated wing induces high vertical turbulent momentum transport near the TE. At the middle portion of the wing, a large region of positive $\langle \overline{u'w'} \rangle$ (Q1 and Q3 types event dominant) can be observed for the smooth wing. This location corresponds to the mean LEV core location in time-averaged streamlines; positive Reynolds stress (Q1 and Q3 types event dominant) corresponds to contribution to negative turbulence production [i.e., TKE sink, energy from fluctuating component is transferred to the mean flow (Metcalfe *et al.*, 1987; Soldati and Banerjee, 1998)]. As a result, turbulent momentum transport in smooth wing is limited compared to the serrated wing. We also show the Reynolds stress in the crossflow plane ($(\langle \overline{u'v'} \rangle / U_\infty^2)$ in Fig. 17. Significant differences in the pattern of the contour are not observed except near the leading edge, which implies that the spanwise fluctuations at the leading edge does not significantly alter turbulent stress pattern in the crossflow plane.

## IV. CONCLUSION

The present study demonstrates the impact of owls' microscale LE serrations on the flow dynamics of an owl wing. Via utilizing the DNS method, the flow around the owl wing with and without serrations is resolved to the smallest scales at 20° AOA with the Reynolds number 40 000. Typically, during landing, takeoff, and prey capture, owls fly at high AOA. However, during takeoff, high AOA is observed accompanied by wing flapping. Our simulation setup can be associated with landing or prey capture phase, while the owl is not flapping. During these stages, owls need to slow down and increased lift is required. Our results show that serrations prompt reduced aerodynamic performance compared to the smooth LE wing (3.2% decrease); however, lift production is enhanced by 2%, which suggests that serration may contribute positively to owls' flight at 20° AOA during the landing and prey capture phase.

Separation bubble is detrimental to aerodynamic performance and stability of flight vehicles, birds, marine animals, etc. (Shyy *et al.*, 2008; Genc *et al.*, 2020). From the time-averaged results, it is found that serrations promote reverse flow weakening and its area reduction. Note that the effectiveness of control surfaces in air vehicles (such as ailerons, flaps, spoilers, etc.) is dependent on the attached flow over them (Rao, 1984; Lochert, 2019). Similarly, birds also have multi-layered covert feathers, which are generally deployed during high AOA maneuvers, landing, takeoff, etc. Some of these covert feathers (i.e., secondary lesser coverts located near the leading edge) are known for enhancing maneuverability in birds' flights (see the brief review by Othman *et al.*, 2023). Serrations having weaker backflow and sustained reattached flow over the wing may be favorable to other control feathers on owls' upper wing surface. We also observe enhanced spanwise momentum transfer with the serrated case, which may be associated with facilitation of the LEV stabilization during flapping flights (Jardin and David, 2014).

From the instantaneous flow visualizations, we observe that both wings have asymmetric wake consisting of unequal strength vortices. The vortex shedding frequency is impacted due to the presence of serrations in the shear layer passage. Streamwise vorticity is developed early in the shear layer while passing through the array of serrations due to the spanwise deflection of the flow. As a result, three dimensionalities emerge earlier in the shear layer of the serrated wing.

Presumably, this impacts the downstream separation vortex formation mechanism so that during the TEV formation and enlargement phase, a stronger SV persists on the upper surface of the wing, which drives more vorticity ejection from the wall. Therefore, the serrated wing depicts larger secondary vortices ($\sim$0.5 z/c) in the time-averaged profiles. Turbulence characteristics of the serrated wing are found to be different compared to what found in the real owl wings with serrations removed (Geyer *et al.*, 2017). We observe an increase in TKE as well as Reynolds stress with the inclusion of serrations, whereas the real owl wings show the opposite trend. This is probably due to other morphological features of the real owl wing. Our findings suggest that serration enhances downward turbulent momentum transport over the wing, especially near the TE where SV and TEV interact mostly over the shedding cycle. It is commonly known that separation bubble formation and its intensity can be controlled via passive and active control methods (i.e., blowing, vortex generators, etc.), which essentially introduce turbulence generation upstream the separation point (see brief review by Jahanmiri, 2011). Although AOA other than 20° has not been investigated in this study, it can be surmised that larger AOAs will have shear layers that will pass through the array of serrations. As turbulent momentum transport is ultimately increased due to this early onset of three dimensionality in the shear layer, it may improve "stall resistance" at larger AOA.

## AUTHOR DECLARATIONS
### Conflict of Interest

The authors have no conflicts to disclose.

### Author Contributions

**Asif Shahriar Nafi:** Conceptualization (equal); Data curation (equal); Formal analysis (equal); Investigation (equal); Methodology (equal); Software (equal); Validation (equal); Visualization (equal); Writing – original draft (equal); Writing – review & editing (equal). **Nikolaos Beratlis:** Investigation (equal); Methodology (equal); Software (equal); Validation (equal); Visualization (equal). **Elias Balaras:** Conceptualization (equal); Investigation (equal); Methodology (equal); Validation (equal); Visualization (equal). **Roi Gurka:** Conceptualization (equal); Formal analysis (equal); Writing – review & editing (equal).

## DATA AVAILABILITY

The data that support the findings of this study are available from the corresponding author upon reasonable request.

## REFERENCES

Abbot, I. H., Doenhoff, E. A., and Stivers, L. S., "Summary of airfoil data," NASA Report No. 824 (1945).

Al-Battal, N., Cleaver, D., and Gursul, I., "Aerodynamic load control through blowing," in 54th AIAA Aerospace Sciences Meeting (2016).

Anderson, G. W., "An experimental investigation of a high lift device on the owl wing," Master's thesis (Air Force Institute of Technology, Wright-Patterson AFB, 1973).

Anyoji, M., Wakui, S., Hamada, D., and Aono, H., "Experimental study of owl-like airfoil aerodynamics at low Reynolds numbers," J. Flow Control, Meas. Visualization **06**, 185–197 (2018).

Bachmann, T., "Anatomical, morphometrical and biomechanical studies of barn owls' and pigeons' wings," Master's thesis (RWTH Aachen University, 2010).

Bachmann, T. and Wagner, H., "The three-dimensional shape of serrations at barn owl wings: Towards a typical natural serration as a role model for biomimetic applications," J. Anat. **219**(2), 192–202 (2011).

Balaras, E., "Modeling complex boundaries using an external force field on fixed Cartesian grids in large-eddy simulations," Comput. Fluids **33**(3), 375–404 (2004).

Balci, A., Andersen, M., Thompson, M. C., and Brùns, M., "Codimension three bifurcation of streamline patterns close to a no-slip wall: A topological description of boundary layer eruption," Phys. Fluids **27**(5), 053603 (2015).

Ben-Gida, H., Gurka, R., and Weihs, D., "Leading-edge vortex as a high-lift mechanism for large-aspect-ratio wings," AIAA J. **58**(7), 2806–2819 (2020).

Beratlis, N., Capuano, F., Krishnan, K., Gurka, R., Squires, K., and Balaras, E., "Direct numerical simulations of a great horn owl in flapping flight," Integr. Comp. Biol. **60**(5), 1091–1108 (2020).

Boutilier, M. H. and Yarusevych, S., "Effects of end plates and blockage on low-Reynolds number flows over airfoils," AIAA J. **50**, 1547–1559 (2012).

Bradshaw, P., "Turbulent secondary flows," Annu. Rev. Fluid Mech. **19**(1), 53–74 (1987).

Breuer, M. and Jovicic, N., "An LES investigation of the separated flow past an airfoil at high angle of attack," in *Direct and Large-Eddy Simulation IV*, ERCOFTAC Series (Kluwer Academic Publishers, 2001a), pp. 165–172.

Breuer, M. and Jovicic, N., "Separated flow around a flat plate at high incidence: An LES investigation," J. Turbul. **2**, N18 (2001b).

Buresti, G., "Bluff-body aerodynamics," in International Advanced School on Wind-Excited and Aeroelastic Vibrations of Structures, Genoa, Italy (2000).

Busse, A., Lützner, M., and Sandham, N. D., "Direct numerical simulation of turbulent flow over a rough surface based on a surface scan," Comput. Fluids **116**, 129–147 (2015).

Cantwell, B. and Coles, D., "An experimental study of entrainment and transport in the turbulent near wake of a circular cylinder," J. Fluid Mech. **136**(1), 321 (1983).

Capuano, F., Beratlis, N., Zhang, F., Peet, Y., Squires, K., and Balaras, E., "Cost vs Accuracy: DNS of turbulent flow over a sphere using structured immersed-boundary, unstructured finite-volume, and spectral-element methods," Eur. J. Mech. B **102**, 91–102 (2023).

Chakraborty, P., Balachandar, S., and Adrian, R. J., "On the relationships between local vortex identification schemes," J. Fluid Mech. **535**, 189–214 (2005).

Chang, J., Zhang, Q., He, L., and Zhou, Y., "Shedding vortex characteristics analysis of NACA 0012 airfoil at low Reynolds numbers," Energy Rep. **8**, 156–174 (2022).

Doligalski, T. L., Smith, C. R., and Walker, J. D. A., "Vortex interactions with walls," Annu. Rev. Fluid Mech. **26**(1), 573–616 (1994).

Duraisamy, K., "Studies in tip vortex formation, evolution and control," Ph.D. thesis (University of Maryland, College Park, 2005).

Eisenbach, S. and Friedrich, R., "Large-eddy simulation of flow separation on an airfoil at a high angle of attack and Re = 105 using Cartesian grids," Theor. Comput. Fluid Dyn. **22**(3–4), 213–225 (2007).

Freymuth, P., Bank, W., and Palmer, M., "Vortices around airfoils: The flow around an airfoil in unsteady wind provides insight into a difficult realm of aerodynamics," Am. Sci. **72**(3), 242–248 (1984).

Genc, M. S., Koca, K., Demir, H., and Açıkel, H. H., "Traditional and new types of passive flow control techniques to pave the way for high maneuverability and low structural weight for UAVs and MAVs," in *Autonomous Vehicles* (IntechOpen, 2020).

Geyer, T. F., Claus, V. T., Hall, P. M., and Sarradj, E., "Silent owl flight: The effect of the leading-edge comb," Int. J. Aeroacoust. **16**(3), 115–134 (2017).

Giuni, M. and Green, R. B., "Vortex formation on squared and rounded tip," Aerosp. Sci. Technol. **29**(1), 191–199 (2013).

Graham, R. R., "The silent flight of owls," J. R. Aeronaut. Soc. **38**, 837–843 (1934).

Guha, A. and Rahmani, M., "Predicting vortex merging and ensuing turbulence characteristics in shear layers from initial conditions," J. Fluid Mech. **878**, R4 (2019).

Hain, R., Kähler, C., and Radespiel, R., "Dynamics of laminar separation bubbles at low-Reynolds-number aerofoils," J. Fluid Mech. **630**, 129–153 (2009).

Hoarau, Y., Braza, M., Ventikos, Y., Faghani, D., and Tzabiras, G., "Organized modes and the three-dimensional transition to turbulence in the incompressible flow around a NACA0012 wing," J. Fluid Mech. **496**, 63–72 (2003).

Huai, W., Xue, W., and Qian, Z., "Large-eddy simulation of turbulent rectangular open-channel flow with an emergent rigid vegetation patch," Adv. Water Resour. **80**, 30–42 (2015).

Huang, R. F., Wu, J. Y., Jeng, J. H., and Chen, R. C., "Surface flow and vortex shedding of an impulsively started wing," J. Fluid Mech. **441**, 265 (2001).

Hunt, J., Wray, A., and Moin, P., "Eddies, stream, and convergence zones in turbulent flows," in *Proceeding of the Summer Program 1988* (Center for Turbulence Research, 1988), pp. 193–208.

Jahanmiri, M., "Laminar separation bubble: Its structure, dynamics and control," Research Report No. 2011:06 (Chalmers University of Technology, 2011).

Jardin, T. and David, L., "Spanwise gradients in flow speed help stabilize leading-edge vortices on revolving wings," Phys. Rev. E **90**(1), 013011 (2014).

Jaworski, J. W. and Peake, N., "Aeroacoustics of silent owl flight," Annu. Rev. Fluid Mech. **52**(1), 395 (2020).

Jeong, J. and Hussain, F., "On the identification of a vortex," J. Fluid Mech. **285**(1), 69 (1995).

Johnson, W., *Rotorcraft Aeromechanics* (Cambridge University Press, 2013).

Jones, L. E., Sandberg, R. D., and Sandham, N. D., "Direct numerical simulations of forced and unforced separation bubbles on an airfoil at incidence," J. Fluid Mech. **602**, 175 (2008).

Kitsios, V., Cordier, L., Bonnet, J.-P., Ooi, A., and Soria, J., "On the coherent structures and stability properties of a leading-edge separated aerofoil with turbulent recirculation," J. Fluid Mech. **683**, 395–416 (2011).

Klan, S., Klaas, M., and Schröder, W., "The Influence of leading-edge serrations on the flow field of an artificial owl wing," in 28th AIAA Applied Aerodynamics Conference, Chicago, Illinois, USA (2010).

Klose, B. F., Spedding, G. R., and Jacobs, G. B., "Direct numerical simulation of cambered airfoil aerodynamics at Re = 20,000," arXiv:2108.04910 (2021).

Krishnan, K., "Aerodynamics and turbulent wake-flow characteristics of owls during flapping flight," Ph.D. thesis (Coastal Carolina University, 2022).

Kroeger, R. A., Gruschka, H. D., and Helvey, T. C., "Low speed aerodynamics for ultra-quiet flight," Technical Report No. AFFDL TR-71-75 (1972).

Kudela, H. and Malecha, Z. M., "Eruption of a boundary layer induced by a 2D vortex patch," Fluid Dyn. Res. **41**(5), 055502 (2009).

Lam, K. M., "Phase-locked eduction of vortex shedding in flow past an inclined flat plate," Phys. Fluids **8**(5), 1159–1168 (1996).

Lawley, J., Ben-Gida, H., Krishnamoorthy, K., Hackett, E. E., Kopp, G. A., Morgan, G., and Gurka, R., "Flow features of the near wake of the Australian boobook owl (Ninox boobook) during flapping flight suggest an aerodynamic mechanism of sound suppression for stealthy flight," Integr. Org. Biol. **1**(1), obz001 (2019).

Lilley, G. M., "A study of the silent flight of the owl," in 4th AIAA/CEAS Aeroacoustics Conference, Toulouse, France (1998).

Linehan, T. and Mohseni, K., "On the maintenance of an attached leading-edge vortex via model bird alula," J. Fluid Mech. **897**, A17 (2020).

Liu, T., Kuykendoll, K., Rhew, R., and Jones, S., "Avian wing geometry and kinematics," AIAA J. **44**(5), 954–963 (2006).

Lochert, P., Huber, K. C., Ghoreyshi, M., and Allen, J., "Control device effectiveness studies of a 53° swept flying wing configuration. Experimental, computational, and modeling considerations," Aerosp. Sci. Technol. **93**, 105319 (2019).

Luton, A., Ragab, S., and Telionis, D., "Interaction of spanwise vortices with a boundary layer," Phys. Fluids **7**(11), 2757–2765 (1995).

McAuliffe, B. R. and Yaras, M. I., "Passive manipulation of separation-bubble transition using surface modifications," J. Fluids Eng. **131**, 16 (2009).

Metcalfe, R. W., Orszag, S. A., Brachet, M. E., and Riley, J. J., "Secondary instability of a temporally growing mixing layer," J. Fluid Mech. **184**, 207–243 (1987).

Nafi, A., Ben-Gida, H., Guglielmo, C. G., and Gurka, R., "Aerodynamic forces acting on birds during flight: A comparative study of a shorebird, songbird and a strigiform," Exp. Therm. Fluid Sci. **113**, 110018 (2020).

Nedic, J. and Vassilicos, J. C., "Vortex shedding and aerodynamic performance of airfoil with multiscale trailing-edge modifications," AIAA J. **53**(11), 3240–3250 (2015).

Ol, M., McCauliffe, B., Hanff, E., Scholz, U., and Kaehler, C., "Comparison of Laminar separation bubble measurements on a low Reynolds number airfoil in three facilities," in 35th AIAA Fluid Dynamics Conference and Exhibit (2005).

Orlanski, I., "Simple boundary-condition for unbounded hyperbolic flows," J. Comput. Phys. **21**, 251–269 (1976).

Othman, A. K., Zekry, D. A., Saro-Cortes, Lee, K. J., and Wissa, A. A., "Aerial and aquatic biological and bioinspired flow control strategies," Commun. Eng. **2**, 30 (2023).

Pal, A., Sarkar, S., Posa, A., and Balaras, E., "Direct numerical simulation of stratified flow past a sphere at a subcritical Reynolds number of 3700 and moderate Froude number," J. Fluid Mech. **826**, 5–31 (2017).

Pauley, W. R. and Eaton, J. K., "Experimental study of the development of longitudinal vortex pairs embedded in a turbulent boundary layer," AIAA J. **26**(7), 816–823 (1988).

Perez-Torro, R. and Kim, J. W., "A large-eddy simulation on a deep-stalled aerofoil with a wavy leading edge," J. Fluid Mech. **813**, 23–52 (2017).

Perry, A. E. and Steiner, T. R., "Large-scale vortex structures in turbulent wakes behind bluff bodies. Part 1. Vortex formation processes," J. Fluid Mech. **174**(1), 233 (1987).

Posa, A. and Balaras, E., "Large eddy simulation of an isolated vertical axis wind turbine," J. Wind Eng. Ind. Aerodyn. **172**, 139–151 (2018).

Posa, A., Parker, C. M., Leftwich, M. C., and Balaras, E., "Wake structure of a single vertical axis wind turbine," Int. J. Heat Fluid Flow **61**, 75–84 (2016).

Posa, A., Vanella, M., and Balaras, E., "An adaptive reconstruction for Lagrangian, direct-forcing, immersed-boundary methods," J. Comput. Phys. **351**, 422–436 (2017).

Rahromostaqim, M., Posa, A., and Balaras, E., "Numerical investigation of the performance of pitching airfoils at high amplitudes," AIAA J. **54**, 2221–2232 (2016).

Rao, C., Ikeda, T., Nakata, T., and Liu, H., "Owl-inspired leading-edge serrations play a crucial role in aerodynamic force production and sound suppression," Bioinspiration Biomimetics **12**(4), 046008 (2017).

Rao, D. M., "Leading edge flap system for aircraft control augmentation," U.S. patent 4,485,992 (4 December 1984).

Robinson, S. K., "Coherent motions in the turbulent boundary layer," Annu. Rev. Fluid Mech. **23**(1), 601–639 (1991).

Shyy, W., Lian, Y., Tang, J., Viieru, D., and Liu, H., *Aerodynamics of Low Reynolds Number Flyers* (Cambridge University Press, 2008).

Smith, C. E., Beratlis, N., Balaras, E., Squires, K., and Tsunoda, M., "Numerical investigation of the flow over a golf ball in the subcritical and supercritical regimes," Int. J. Heat Fluid Flow **31**(3), 262–273 (2010).

So, J., Ryan, K., and Sheard, G. J., "Interaction of an unequal-strength vortex pair," in Proceedings of the 16th Australasian Fluid Mechanics Conference, Crown Plaza, Gold Coast, Queensland, Australia (2007).

Soldati, A. and Banerjee, S., "Turbulence modification by large-scale organized electrohydrodynamic flows," Phys. Fluids **10**(7), 1742–1756 (1998).

Spedding, G. R. and McArthur, J., "Span efficiencies of wings at low Reynolds numbers," J. Aircr. **47**(1), 120–128 (2010).

Strawn, R. C., Kenwright, D. N., and Ahmad, J., "Computer visualization of vortex wake systems," AIAA J. **37**(4), 511–512 (1999).

Swalwell, K., Sheridan, J., and Melbourne, W., "Frequency analysis of surface pressures on an airfoil after stall," in 21st AIAA Applied Aerodynamics Conference (2003).

Taira, K. and Colonius, T., "Three-dimensional flows around low-aspect-ratio flat-plate wings at low Reynolds numbers," J. Fluid Mech. **623**, 187 (2009).

Torenbeek, E., Wittenberg, H., and Calvert, S., *Flight Physics: Essentials of Aeronautical Disciplines and Technology, with Historical Notes* (Springer, 2009).

Townsend, A., Jiya, I. N., Martinson, C., Bessarabov, D., and Gouws, R., "A comprehensive review of energy sources for unmanned aerial vehicles, their shortfalls, and opportunities for improvements," Heliyon **6**(11), e05285 (2020).

Visbal, M. R., "Numerical investigation of deep dynamic stall of a plunging airfoil," AIAA J. **49**(10), 2152–2170 (2011).

Wagner, H., Weger, M., Klaas, M., and Schröder, W., "Features of owl wings that promote silent flight," Interface Focus **7**(1), 20160078 (2017).

Wallace, J. M., "Quadrant analysis in turbulence research: History and evolution," Annu. Rev. Fluid Mech. **48**(1), 131–158 (2016).

Wallace, J. M., Brodkey, R. S., and Eckelmann, H., "The wall region in turbulent shear flow," J. Fluid Mech. **54**, 39–48 (1972).

Wang, Y., Zhao, K., Lu, X.-Y., Song, Y.-B., and Bennett, G. J., "Bio-inspired aerodynamic noise control: A bibliographic review," Appl. Sci. **9**(11), 2224 (2019).

Weger, M. and Wagner, H., "Morphological variations of leading-edge serrations in owls (Strigiformes)," PLoS One **11**(3), e0149236 (2016).

Winzen, A., Roidl, B., Klän, S., Klaas, M., and Schröder, W., "Particle-image velocimetry and force measurements of leading-edge serrations on owl-based wing models," J. Bionic Eng. **11**(3), 423–438 (2014).

Yang, J., "An embedded-boundary formulation for large-eddy simulation of turbulent flows interacting with moving boundaries," Ph.D. thesis (University of Maryland, 2005).

Yang, J. and Balaras, E., "An embedded-boundary formulation for large-eddy simulation of turbulent flows interacting with moving boundaries," J. Comput. Phys. **215**(1), 12–40 (2006).

Yang, Z., "Numerical study of instabilities in separated–reattached flows," Int. J. Comput. Methods Exp. Meas. **1**(2), 116–131 (2013).

Yang, Z. and Voke, P. R., "Large-eddy simulation of boundary-layer separation and transition at a change of surface curvature," J. Fluid Mech. **439**, 305 (2001).

Yarusevych, S. and Boutilier, M. S. H., "Vortex shedding of an airfoil at low Reynolds numbers," AIAA J. **49**(10), 2221–2227 (2011).

Yarusevych, S., Kawall, J. G., and Sullivan, P. E., "Separated-shear-layer development on an airfoil at low Reynolds numbers," AIAA J. **46**(12), 3060–3069 (2008).

Yarusevych, S., Sullivan, P. E., and Kawall, J. G., "On vortex shedding from an airfoil in low-Reynolds-number flows," J. Fluid Mech. **632**, 245 (2009).

Zaman, K. B. M. Q., Mckinzie, D. J., and Rumsey, C. L., "A natural low-frequency oscillation of the flow over an airfoil near stalling conditions," J. Fluid Mech. **202**(1), 403 (1989).

Zauner, M., De Tullio, N., and Sandham, N. D., "Direct numerical simulations of transonic flow around an airfoil at moderate Reynolds numbers," AIAA J. **57**, 597–511 (2019).

Zhang, W. and Samtaney, R., "Assessment of spanwise domain size effect on the transitional flow past an airfoil," Comput. Fluids **124**, 39–53 (2016).

04 January 2024 17:15:29